Complex 3-D surface deformation in the 1971 San Fernando, California earthquake reveals static and dynamic controls on off-fault deformation

Élyse Gaudreau[1], James Hollingsworth[2], Edwin Nissen[1], and Gareth Funning[3]

[1]University of Victoria
[2]Université Grenoble Alpes
[3]University of California, Riverside

November 22, 2022

Abstract

The shallow 1971 Mw 6.6 San Fernando, California earthquake involved a complex rupture process on an immature thrust fault with a non-planar geometry, and is notable for having a higher component of left-lateral surface slip than expected from seismic models. We extract its 3-D coseismic surface displacement field from aerial stereo photographs and document the amount and width of the vertical and strike-parallel components of distributed deformation along strike. The results confirm the significant left-lateral surface offsets, suggesting a slip vector rotation at shallow depths. Comparing our offsets against field measurements of fault slip, we observe that most of the offset was accommodated in the damage zone, with off-fault deformation averaging 68% in both the strike-parallel and vertical components. However, the magnitude and width of off-fault deformation behave differently between the vertical and strike-parallel components, which, along with the rotation in rake near the surface, can be explained by dynamic rupture effects.

Complex 3-D surface deformation in the 1971 San Fernando, California earthquake reveals static and dynamic controls on off-fault deformation

É. Gaudreau[1], J. Hollingsworth[2], E. Nissen[1], G.J. Funning[3]

[1]University of Victoria, Victoria, Canada
[2]ISTerre, Université Grenoble-Alpes, Grenoble, France
[3]University of California Riverside, Riverside, USA

Key Points:

- 3-D coseismic deformation field of the 1971 San Fernando earthquake is one of the earliest imaged using correlation of aerial photographs
- Off-fault deformation is partitioned between the strike-parallel and vertical components of deformation
- Primary controls of off-fault deformation are different for the strike-parallel and vertical components

Corresponding author: É. Gaudreau, gaudreau@uvic.ca

Abstract

The shallow 1971 M_W 6.6 San Fernando, California earthquake involved a complex rupture process on an immature thrust fault with a non-planar geometry, and is notable for having a higher component of left-lateral surface slip than expected from seismic models. We extract its 3-D coseismic surface displacement field from aerial stereo photographs and document the amount and width of the vertical and strike-parallel components of distributed deformation along strike. The results confirm the significant left-lateral surface offsets, suggesting a slip vector rotation at shallow depths. Comparing our offsets against field measurements of fault slip, we observe that most of the offset was accommodated in the damage zone, with off-fault deformation averaging 68% in both the strike-parallel and vertical components. However, the magnitude and width of off-fault deformation behave differently between the vertical and strike-parallel components, which, along with the rotation in rake near the surface, can be explained by dynamic rupture effects.

Plain Language Summary

The 1971 San Fernando, California earthquake is infamous for its strong ground motions and large lateral fault offsets measured in the field, despite the compressional tectonic stresses that nucleated the earthquake at depth. We produce maps of the 3-D surface deformation that occurred during the earthquake by comparing pre-earthquake and post-earthquake aerial photographs of the rupture area. The results confirm the presence of important lateral and compression-driven slip at the surface. This surface offset was distributed over a wide damage zone, and as such, previously reported offset measurements did not capture the total slip that occurred at the surface. Underestimating total slip has impacts for seismic hazard assessments; understanding the factors that control how distributed or localized surface deformation is provides insight into earthquake behavior and helps improve our estimates of the seismic hazard. Our results show that during the San Fernando earthquake, lateral and compression-driven slip behaved differently within the damage zone, which may suggest that the two slip components were affected by different factors and damage generation mechanisms.

1 Introduction

Fault maturity is thought to play a significant role in the behavior of earthquakes, including rupture velocity (e.g., Harrington & Brodsky, 2009; Bruhat et al., 2016; Perrin et al., 2016), rupture length (Wesnousky, 1988, 1990; Manighetti et al., 2007; Huang, 2018), seismicity (Wesnousky, 1990; Harrington & Brodsky, 2009; Thakur et al., 2020), ground motion (Radiguet et al., 2009; Thomas, M.Y. and Bhat, H.S. and Klinger, Y., 2017), the distribution and magnitude of surface slip (Bürgmann et al., 1994; Manighetti et al., 2007; Candela et al., 2012; Perrin et al., 2016; Bruhat et al., 2020; Pousse-Beltran et al., 2020), and the amount of diffuse deformation that occurs in the damage zone on either side of the main slip surfaces (Dolan & Haravitch, 2014; Milliner et al., 2015; Perrin et al., 2016). Although there is no single metric for the maturity of a particular fault due to the many factors that affect fault evolution (e.g. cumulative slip, varying fault healing rates), faults are generally considered immature if they have not hosted many earthquakes and as a result have not yet developed an efficient system for localizing deformation (Ben-Zion & Sammis, 2003; Dolan & Haravitch, 2014). Common characteristics of immature faults include a high density of bends and steps (Wesnousky, 1988, 1990; Manighetti et al., 2007), a coseismic shallow slip deficit (Dolan & Haravitch, 2014), a heterogeneous stress field and slip distribution (Bürgmann et al., 1994; Manighetti et al., 2007), and delocalized deformation (Dolan & Haravitch, 2014; Milliner et al., 2015; Perrin et al., 2016). Studying the behavior of immature faults is vital for seismic hazard assessments as the hazard around these faults is often underestimated until a strong and potentially damaging earthquake occurs (e.g., Jackson et al., 2006; Quigley et al., 2012; Gaudreau et al., 2019). Moreover, since immature faults are associated with deformation distributed tens of meters to kilometers beyond the main slip surfaces, fault offsets observed in the field are typically limited to offsets on the main slip surfaces and fall short of the total coseismic offset, resulting in an underestimation of the fault's slip rate and seismic hazard (e.g., Milliner et al., 2015; Cheng & Barnhart, 2021).

In this study, we use the term 'off-fault deformation' (OFD) to refer to the deformation that occurs in the wide (tens of meters to kilometers) zone of damaged rock around the high-strain fault core. This includes deformation accommodated by micro- and macrofracturing, warping, granular flow, and block rotation, and consists of both elastic and inelastic deformation (e.g. Milliner et al., 2015; Scott et al., 2018; Cheng & Barnhart, 2021). Distributed deformation in the shallow crust is thought to be one of the factors causing apparent shallow slip deficits, the systematic reduction in shallow crustal slip based on geodetic elastic dislocation models (e.g. Fialko et al., 2005; Kaneko & Fialko, 2011; Xu et al., 2016). Different mechanisms contribute towards OFD generation during an earthquake, such as the formation of a cloud of microcracks around the rupture tip as it propagates (Martel et al., 1988; Lockner et al., 1991; Lyakhovsky et al., 1997), seismic waves propagating ahead of the rupture front (Ma, 2008; Thomas & Bhat, 2018; Jara et al., 2021) and the zone of high strain rate around the dynamically-propagating rupture front (Andrews, 1976; Poliakov et al., 2002; Rice et al., 2005). Moreover, stress heterogeneities caused by continued slip on a rough fault surface after the passage of the rupture front generate additional off-fault damage (Chester & Chester, 2000; Dieterich & Smith, 2009).

We assess the role of structural complexity, fault segment maturity and near-surface geological material on the distribution of OFD. Straighter, structurally simpler and more mature fault segments, as well as stronger near-surface materials tend to promote more uniform slip and localized deformation, and thick, undeformed sediments and partially indurated sedimentary rocks are thought to delocalize deformation (Dolan & Haravitch, 2014; Zinke et al., 2014; Milliner et al., 2015; Roten et al., 2017). Other factors commonly affecting OFD distribution include damage inherited from previous earthquakes (e.g., Fialko et al., 2002; Zinke et al., 2014; Cochran et al., 2009). The oblique 1971 San Fernando, California earthquake is a well-known case study of a destructive rupture on an immature fault not previously considered active and featured strong ground motions (Wentworth et al., 1971). Here, we extract its 3-D coseismic deformation field from high resolution stereo aerial photographs in order to assess the complex surface deformation, and the factors controlling the width and amount of distributed deformation. Of particular interest is the effect that the thrust component of slip has on the distribution and width of OFD, since most of the aforementioned studies focus on strike-slip earthquakes, and surface-rupturing thrust earthquakes are relatively uncommon. We use a workflow involving NASA's Ames Stereo Pipeline software (Beyer et al., 2018), the ENVI plugin Co-registration of Optically Sensed Images and Correlation (COSI-Corr) (Leprince et al., 2007) and MATLAB scripts to map 3-D coseismic deformation from high-resolution stereo aerial photographs. Offsets and OFD magnitude and width are measured by profiling the displacement field at regular intervals along strike. Their distribution along with changes in fault geometry and geology allow us to explore which factors may control the surface expression of near-fault coseismic deformation. Notably, spatial patterns of OFD magnitude and deformation zone widths are different in the strike-parallel and vertical components, which may reflect the complexity of the rupture and the combination of static and dynamic processes affecting these parameters.

2 Tectonic Setting and Fault Structure

The WNW-striking, north-dipping San Fernando Fault is located in the Transverse Ranges of California, USA, in the transpressional region south of the San Andreas Fault's

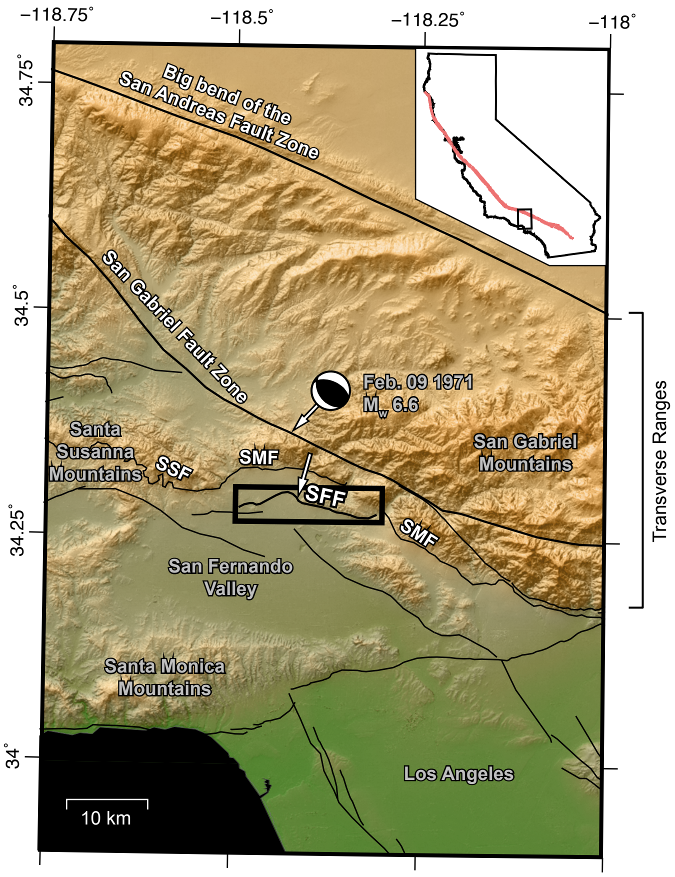

Figure 1. Active fault map around the San Fernando area. Thin black lines are surface faults from the U.S. Geological Survey Quaternary Fault and Fold Database (https://doi.org/10.5066/F7S75FJM) and Whitcomb et al. (1973) determined the focal mechanism from P-wave first motions. White arrows show slip vector azimuths for the deeper and shallower portions of the rupture based on local and teleseismic waveform modelling (Heaton, 1982). Rectangle shows location of Figure 2A. SSF: Santa Susana Fault; SMF: Sierra Madre Fault; SFF: San Fernando Fault. Inset shows the location of the main figure (black rectangle) and San Andreas Fault (red line) within the state of California.

"big bend" (Figure 1). The Transverse Ranges are characterized by substantial late Cenozoic north-south shortening and numerous east-west strike-slip and thrust faults (Wentworth et al., 1971). The surface ruptures from the 1971 earthquake are situated in the San Fernando Valley, part of the Greater Los Angeles area, which is bounded to the north by the Santa Susana and San Gabriel Mountains, and to the south by the Santa Monica Mountains. The compressional axis of the regional stress field is oriented N-S to NNE-SSW (e.g., Stein et al., 1994). The San Gabriel Mountains are the result of 5–10 million years of thrusting on structures such as the Sierra Madre and Santa Susana Faults (Figure 1). Despite the presence of many young faults in the San Gabriel Mountains, the San Fernando area was characterized by scarce seismicity prior to the 1971 earthquake (Wentworth et al., 1971), with less than 10 earthquakes larger than magnitude 4.0 recorded in and around the San Fernando Valley (USGS COMCAT catalog; https://earthquake.usgs.gov/earthquakes/search/). Before 1971, the most notable event in the region is the historical Pico Canyon earthquake of 1893, for which there were reports of strong shaking and multiple landslides (Townley & Allen, 1939). As a result, the San Fernando Fault and many others in the San Gabriel Mountains were either unknown or not widely considered to be active at the time (Wentworth et al., 1971; Weber, 1975, and references therein).

The 1971 surface rupture consists of two north-dipping main segments — the west-striking Sylmar segment cross-cutting the San Fernando valley, and to the east, the WNW-striking Tujunga segment, a valley-bounding fault south of the San Gabriel Mountains — offset by a 1.3 km right step (Figure 2A; Wentworth et al., 1971). Secondary surface ruptures identified after the earthquake include the Sylmar Basin secondary fault in the footwall which is sub-parallel to the main strand's Sylmar segment, and the Kagel Canyon secondary fault that cuts across the San Gabriel Mountains at a 30° angle from the main Tujunga segment. Farther east is the Little Tujunga Canyon secondary fault, sub-parallel to the main fault to the south (Figure 2A). These fault segments are thought to represent an increase in fault complexity near the surface (e.g., Savage et al., 1975; Carena & Suppe, 2002). At depth, the San Fernando Fault cuts through dense, crystalline basement (Wentworth et al., 1971; Tsutsumi & Yeats, 1999; Langenheim et al., 2011). Near the surface, the Sylmar segment cuts through $\sim$4 to 5 km of sedimentary rocks, including moderately indurated Late Miocene and Early Pliocene sandy siltstone, sandstone and shale overlain by undeformed and partially indurated Pleistocene conglomerate, and alluvium (Wentworth et al., 1971; Langenheim et al., 2011). The Tujunga segment cuts through crystalline basement and $\sim$1 to 1.5 km of the Late Miocene siltstone and sandstone formation (Langenheim et al., 2011). The fault seems to follow bedding planes near the surface, with the Sylmar segment dipping 55° to 60° and the Tujunga segment $\sim$25° (Kamb et al., 1971; Barrows, 1975; Sharp, 1975; Weber, 1975; Tsutsumi & Yeats, 1999).

The Sylmar segment coincides with a $>$ 8 m-high pre-existing fault scarp, but paleoseismic investigations were limited due to a lack of near-surface bedding (Weber, 1975). On the other hand, a trench that was excavated across the Lopez Canyon secondary fault (see Figure 2A) showed evidence of $\sim$1 m of slip prior to the San Fernando earthquake, which occurred between 100 and 300 years ago and is thought to have involved rupture of the entire San Fernando fault system (Bonilla, 1973). Further east, in the Tujunga segment, a paleoseismic trench uncovered a slip surface dipping 30°, and $>$13 m of Tertiary sedimentary rocks overlying undated alluvium, indicative of recent faulting (Barrows, 1975). Due to the scarcity of information on the slip history of the San Fernando Fault, we interpret the Tujunga segment as more mature than the Sylmar segment because of its greater hanging wall topography (its surface rupture lies along the foothills of the San Gabriel Mountains: Figure 2A).

The 1971 San Fernando earthquake ruptured one of multiple splays off a north-dipping decollement that continues further south (Fuis et al., 2003). The focal mechanism in Figure 1 was determined by Whitcomb et al. (1973) using P-wave first motions, and thus only represents the initial slip. It is generally agreed upon that the down-dip structure

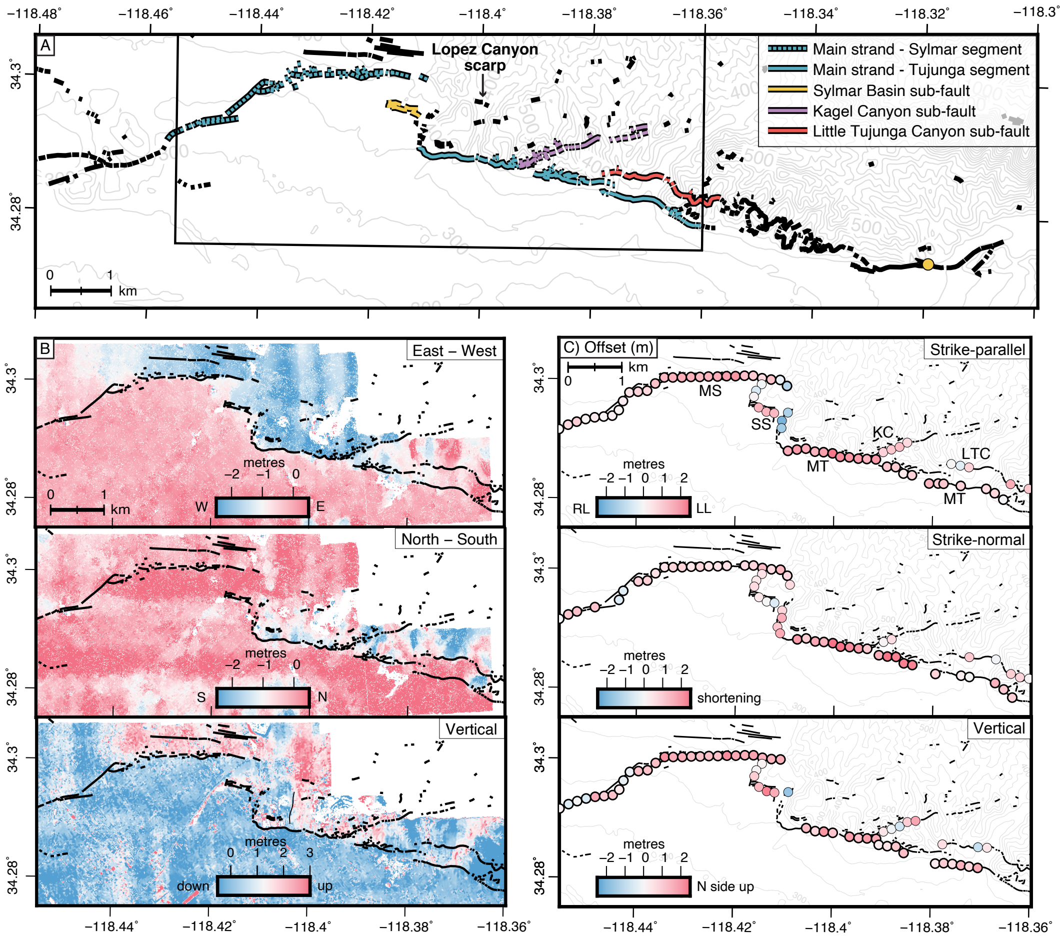

Figure 2. A) Surface rupture of the 1971 San Fernando earthquake (USGS Quaternary fault and fold database of the United States; https://www.usgs.gov/programs/earthquake-hazards/faults; Bonilla et al., 1971; Wentworth et al., 1971; Proctor et al., 1972; Kahle, 1975). Rectangle corresponds to the area analyzed using aerial photographs. Gray contour lines show the topography in meters: the Sylmar segment in the west cuts through the San Fernando basin, while the Tujunga segment intersects the surface at the foothills of the San Gabriel Mountains. Yellow circle: location in Kahle (1975) where curved slickenlines recorded initial left-lateral slip then thrust-oriented slip. Curved slickenlines were also found by Bonilla et al. (1971) at the Lopez Canyon scarp although no interpretation was reported. B) Coseismic displacement field of the 1971 San Fernando earthquake from optical image correlation and DEM differencing. Thin north-south-oriented line in the vertical panel traces the zone of vertical offset mapped by Barrows et al. (1975) (see section 4.1). C) Offset measurements from strike-perpendicular displacement profiles. Circles with thick outlines correspond to measurements on main fault strands used for averages in sections 4 and 5.

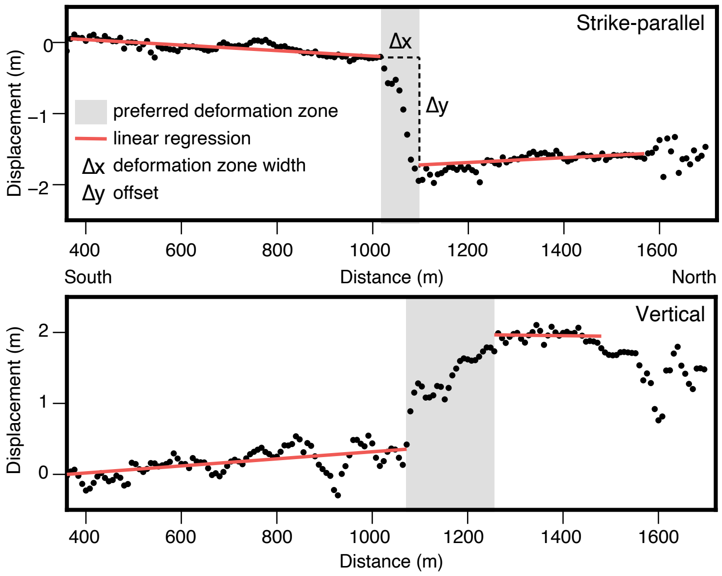

Figure 3. Example strike-perpendicular profile showing the strike-parallel and vertical components of the preferred deformation zone, linear regressions and offset (profile 16: see Supplementary Figure S1).

must be more complex than a single fault plane (e.g., Whitcomb et al., 1973), as the surface projections of such models are not consistent with the location of the observed surface rupture trace. Furthermore, teleseismic waveform modelling studies have demonstrated the complexity of the rupture with moment tensor solutions that have high CLVD components for a single point source (Barker & Langston, 1982; Kim, 1989). Multiple studies propose an evolving seismic source where the deeper slip has an oblique rake of 76° to 84° and the slip shallower than ∼5 to 8 km has a rake of 89° or 90° (Figure 1; Langston, 1978; Heaton & Helmberger, 1979; Heaton, 1982; Kim, 1989). These models include either A) a fault where the dip changes with depth (e.g., Langston, 1978; Heaton & Helmberger, 1979; Carena & Suppe, 2002), or B) two subparallel faults, one surface rupturing and the other a deeper and buried rupture (Heaton, 1982; Kim, 1989). Aftershock relocations form a plane that dips ∼40° (Mori et al., 1995) and nodal planes from moment tensor solutions of the deeper segments dip between 29° and 54° (Langston, 1978; Heaton, 1982; Kim, 1989).

Contrary to the seismic data indicating that the bulk of the slip style was thrust, field data and horizontal control geodetic surveys collected in the 1960s and 1970s indicate left-lateral coseismic surface offsets that are roughly equivalent in amplitude to the vertical offsets, reaching ∼1.9 m on the Sylmar segment (e.g. Bonilla et al., 1971; Kamb et al., 1971; Meade & Miller, 1973; Barrows et al., 1973; Savage et al., 1975). The surface rupture traces were discontinuous but well-defined, although fault surface exposures were rare and thus most slip measurements were made using offset surface features and visual projection of scarp heights (e.g., Bonilla et al., 1971; Kamb et al., 1971; Sharp, 1975). Field teams noted much more slip variability over short distances along the Tujunga segment than the Sylmar segment. Offset measurement challenges included landsliding, roadwork, lack of exposure because of vegetation and buildings, and streets and sidewalks accommodating deformation differently than the underlying geology (Bonilla et al., 1971; Kamb et al., 1971; Barrows, 1975; Sharp, 1975). These difficulties further motivate the application of novel remote sensing techniques to better characterize the surface deformation.

3 Methods

3.1 Digital Elevation Model Generation and Image Orthorectification

We obtained high-resolution scans of historical stereo aerial photographs of the study area acquired in 1969 and 1972 from the United States Geological Survey's Center for Earth Resources Observation and Science (EROS; http://earthexplorer.usgs.gov). The scope of the pre-earthquake aerial survey was to image the San Fernando Valley, therefore providing limited coverage of the hanging wall: other pre-earthquake datasets that had broader coverage suffered greatly in terms of striping artifacts and other sources of noise. We reduced errors created by scanning by first rotating and cropping the photographs such that the corner fiducials were located at the corners of the scan. We enhanced the image contrast using contrast-limited adaptive histogram equalization, and applied a Gaussian blur ($\sigma = 0.5$) to reduce speckle.

To orthorectify the photographs, we produced pre-earthquake and post-earthquake DEMs using the open-source photogrammetry software Ames Stereo Pipeline (ASP), which has extensive documentation and applications in digital Earth observation datasets, historical (scanned film) datasets as well as Lunar and Martian images (Beyer et al., 2018). Orthorectification accuracy depends on the accuracy of the area of interest's topography, the position and orientation of the camera, as well as the camera's intrinsic parameters including focal length, principal point and distortion coefficients. Since historical imagery usually has very limited metadata, the ASP workflow for processing historical imagery begins by computing estimates for each camera's extrinsic parameters. This is done using the THEIA Structure from Motion library (http://www.theia-sfm.org/index.html) invoked from ASP, given initial intrinsic parameter values which are fixed in this step (in this study, the U.S. Geological Survey (USGS) provided the initial estimates for focal lengths, and we assumed the optical centre to be in the centre of the cropped and rotated image). We then use ASP to perform a bundle adjustment with ground control points collected using SRTM as a reference DEM to estimate absolute camera positions (Ajorlou et al., 2021).

We further refine the intrinsic and extrinsic parameters of each camera by collecting dense and uniformly distributed match points between overlapping images, and using these in subsequent bundle adjustments where intrinsic and extrinsic parameters for multiple cameras in the dataset are jointly optimized. The stereo reconstruction (i.e., DEM-creation) process is performed using images that are projected onto a reference DEM, and ASP's MGM Final stereo matching algorithm. Normally the reference DEM has a much coarser resolution than the aerial photographs, which supplies the stereo reconstruction with the long-wavelength topography of the area of interest; however, due to the highly varied topography of the study region, we use a 1-m lidar DEM (USGS 3D Elevation Program; https://www.usgs.gov/core-science-systems/ngp/3dep) since lower resolution reference DEMs lead to great inaccuracies in the stereo reconstruction. The use of a high-resolution reference DEM may add to the high-frequency noise of the DEMs generated. The resulting point clouds may be shifted in space from the reference DEM, and therefore are then aligned to the reference DEM using an iterative closest point algorithm (using the libpointmatcher library, invoked from ASP; https://github.com/ethz-asl/libpointmatcher). We obtained optimal results when we aligned the point clouds from each stereo pair independently to the reference DEM, and a subsequent bundle adjustment jointly optimized the camera parameters for all cameras. Bundle adjustments are most successful in jointly optimizing multiple cameras when there is large (e.g. 60%) overlap between adjacent photographs. However, a joint optimization may be performed over multiple flight lines by collecting interest points in the side lap. This optimization may suffer due to errors introduced by the large perpendicular baseline between flight lines resulting in greater stereoscopic differences, and by illumination differences due to the passage of time between flight lines. Moreover, the overlap area is small (e.g. $< 30\%$), and scanning artifacts introduce additional errors (the latter also affect bundle adjustments of 60% overlap stereo pairs). In this case, we find bundle adjustment is most successful when the joint optimization of the cameras is performed initially for each flight line separately, then a subsequent bundle adjustment is invoked to jointly refine the cameras in all flight lines, improving the co-registration accuracy between the flight lines. We orthorectified the photographs using the optimized camera parameters and the pre-earthquake and post-earthquake DEMs produced using the photographs themselves. The final ground resolution of the orthophotos and DEMs is 1 m.

3.2 Extraction of Horizontal and Vertical Displacement Field Components

Once the pre-earthquake and post-earthquake orthomosaics are created using ASP, we measured the lateral coseismic displacements using COSI-Corr (Leprince et al., 2007; Milliner et al., 2015; Ajorlou et al., 2021). We used a multiscale sliding correlation window of 256 by 256 pixels to 32 by 32 pixels for the correlation, with a step size of 8 pixels, resulting in 8 m-resolution images that represent the eastward and northward components of displacement.

We measured the vertical coseismic displacement field using the pre-earthquake and post-earthquake DEMs created using ASP; however, simply differencing the DEMs does not isolate the vertical component of displacement when there is also a horizontal component (e.g., Oskin et al., 2012; Barnhart et al., 2019). In this study, we measured the vertical component by (1) downsampling the pre-earthquake and post-earthquake DEMs to the same grid as the COSI-Corr displacement maps. Using a MATLAB code, we then calculated the vertical displacement for each pixel by (2) resampling and (3) warping the pre-earthquake DEM such that the pre-earthquake topography is shifted based on the amount of lateral coseismic displacement from our COSI-Corr displacement maps, then (4) subtracting this grid from the post-earthquake DEM.

We masked outliers and pixels where the optical image correlation signal-to-noise ratio is <0.97 (Leprince et al., 2007). We used the detrending tool in COSI-Corr. to remove a second-order polynomial trend which does not impact the near-field offset estimate, and corrected undulating artifacts by sampling the undulations away from the rupture and subtracting the average from the displacement field. We used the Non-Local Means tool in COSI-Corr to denoise the displacement field using a noise parameter of $\sim$0.7, a search area dimension of 21 $\times$ 21 pixels, and a patch size of 5 $\times$ 5 pixels. We estimate the precision of the resulting displacement field from the standard deviation in a stable area of the displacement maps as 0.16 m for the east-west component, 0.27 m for the north-south component, and 0.64 m for the vertical component.

3.3 Coseismic Offset and Distributed Deformation Measurements

To quantify offsets along the length of the main fault and secondary strands, we extract strike-parallel, -normal and vertical displacement profiles oriented perpendicular to the simplified fault traces at regular intervals along strike. For each profile, we first rotated the E-W and N-S displacements into components parallel and normal to the local fault strike. We consider previously mapped secondary faults in the San Fernando area as separate, discrete fault strands rather than distributed deformation around the main fault strand. The profiles are 2 km-long, are regularly-spaced 21 pixels (168 m) apart and are the average of 21 pixel-wide swaths such that each measurement is independent from its neighbors. We discarded the profiles for which the displacement trends are obscured by decorrelation or noise. In some areas that are decorrelated near the surface rupture, we use 25 pixel-wide swaths.

We consider the deformation zone as the zone around the fault within which displacements start to deviate from their far-field trends. We manually picked minimum, maximum and preferred deformation zone width measurements for all profiles that have a high signal-to-noise ratio near the fault. We chose preferred deformation zone boundaries as the location where the deviation from the far-field trend near the fault can no longer be explained by noise. Linear regressions are fitted to the trends in displacement on either side of the preferred deformation zone (Figure 3). We measured offsets by differencing the linear regression values at the extremities of the deformation zone.

We measured the magnitude of OFD at each by subtracting the maximum localized offsets measured in the field located within one profile swath from the total offset measured by profiling the displacement field either side of the fault zone. We then normalize this value to the total offset to obtain the percentage of off-fault deformation (%OFD). The off-fault deformation measurements presented in Figure 4B and Supplementary Tables S1 and S2 include elastic and inelastic off-fault deformation (e.g., Milliner et al., 2015; Scott et al., 2018; Zinke et al., 2019). We do not attempt to isolate the inelastic component of deformation because the noise level and resolution of the data preclude us from reliably measuring strain within the fault zone (e.g., Scott et al., 2018; Barnhart et al., 2019; Milliner et al., 2021). We use localized near-fault measurements taken from detailed field surveys conducted in the days following the earthquake that measured shortening, strike-parallel and vertical offsets (Bonilla et al., 1971; Kamb et al., 1971; Barrows et al., 1973; Sharp, 1975). In areas of highly distributed deformation, the field offset measurements reported are the cumulative displacement over a 50 m-wide (Kamb et al., 1971) or 200 m-wide zone (Bonilla et al., 1971), whereas elsewhere discrete offsets were measured on well-defined fault scarps. For the purposes of measuring %OFD, we chose near-field (within a 50 m-wide zone; e.g., Scott et al., 2018) field measurements.

4 Results

4.1 3-D Coseismic Displacements

The 3-D coseismic displacement results (Figure 2B) reveal a large component of left-lateral offset, consistent with previously published field and trilateration data (Bonilla et al., 1971; Kamb et al., 1971; Meade & Miller, 1973; Savage et al., 1975), but the higher spatial resolution obtained from image correlation and DEM differencing is indispensable for assessing the spatial distribution of near-field deformation and estimating the amount of off-fault deformation (section 4.3). Some of the limitations of processing of historical aerial photographs are noticeable in Figure 2B; striping artifacts (north-south-oriented stripes in the east-west and vertical displacement components, east-west-oriented stripes in the north-south displacement component) were significantly, although not completely reduced. The north-south component of the tectonic signal is affected by additional long-wavelength noise because this component is perpendicular to the flight line and the tectonic signal is biased by the striping artifacts that are roughly parallel to the fault strike. Therefore, we focus on the fault-parallel and vertical components of displacement. In all three dimensions, noise is much greater in the hanging wall of the Tujunga segment, likely introduced by the varied topography of the San Gabriel Mountains and anthropogenic changes that occurred between aerial photograph and reference DEM data acquisitions affecting the DEM generation and orthorectification steps. This heavily affected the region between longitudes -118.365 and -118.342 in the vertical component, and thus offsets were not measured in this area (Supplementary Figure S3). The part of the San Fernando Fault shown in Figure 2B (the area used in this study) hosted the most slip and has a higher density of field measurements.

4.2 Near-Field Coseismic Offsets

All strike-perpendicular profiles with their deformation zone picks and linear regressions are included in Supplementary Figure S2. Surface offsets on the Sylmar segment of the main fault rupture have roughly equal left-lateral and vertical components,

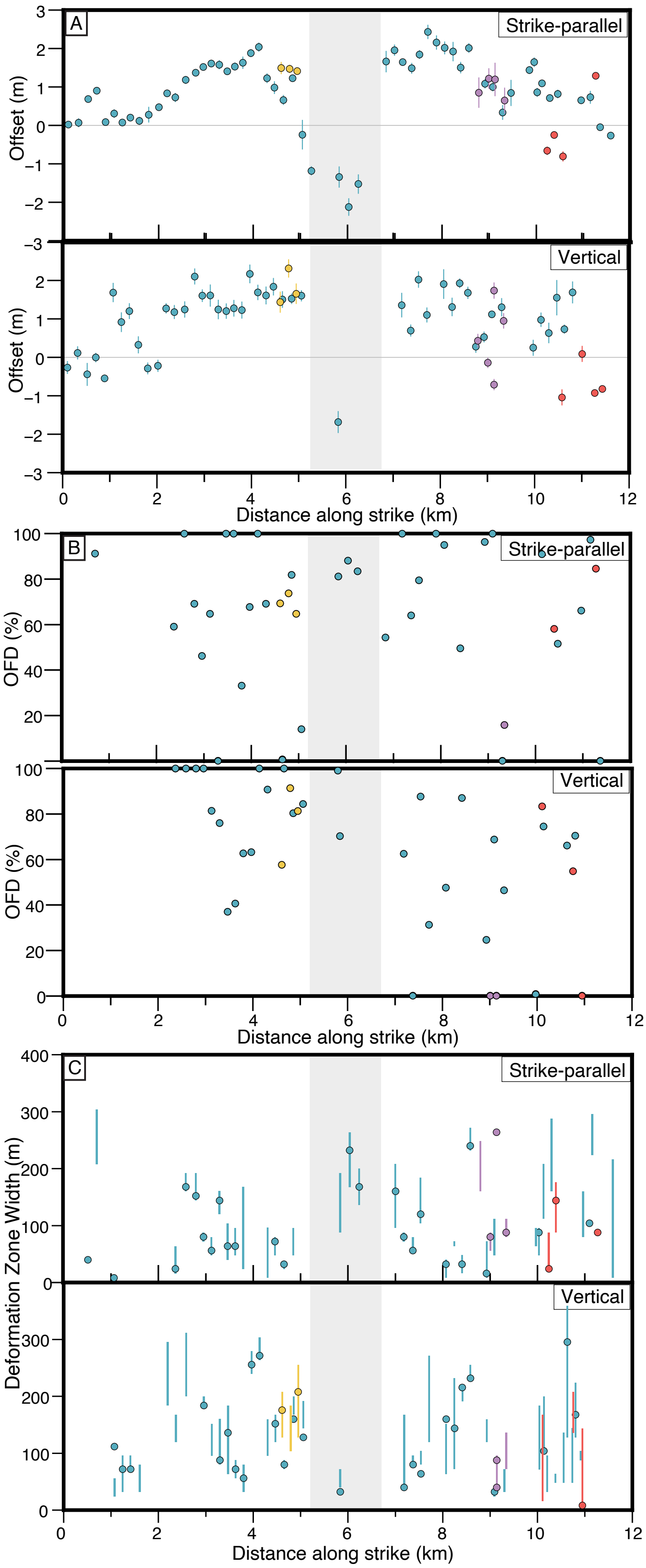

Figure 4. A) Offset measurements plotted as a function of distance along strike: left-lateral slip and hanging wall uplift are positive. Colours correspond to those of discrete fault segments in Figure 2A. Shaded area represents the tear fault separating the Sylmar and Tujunga sections of the main fault. B) %OFD as a function of distance along strike. C) Vertical lines span the minimum and maximum deformation widths, plotted as a function of distance along strike.

reaching a maximum of 2.0 m and 2.2 m respectively, and 2.2 m and 2.0 m in the Tujunga segment. The north-south tear fault connecting the two segments is dominated by right-lateral slip; however, a north-south zone of diffuse deformation ∼800 m to the east is accommodating most of the vertical component of deformation at the bend connecting the Sylmar and Tujunga segments (Figure 2B). Barrows et al. (1975) mapped vertical deformation at this location but were unable to determine whether it occurred during the earthquake. The largest left-lateral and vertical offsets in the Sylmar and Tujunga segments occur on the relatively straight parts of the fault where slip is not distributed onto secondary faults (Figures 2C, 4A). The Sylmar Basin secondary fault accommodates up to 1.5 m and 2.3 m of left-lateral and vertical slip, respectively. The Kagel Canyon and Little Tujunga Canyon secondary fault offsets are irregular, with the former dominated by left-lateral slip while the latter is dominated by shortening.

4.3 Off-Fault Deformation

The average %OFD (± standard deviations) for the strike-parallel and vertical components are 68 ± 32 %, and 68 ± 28 %, respectively (Figure 4B). Since the Sylmar and Tujunga segments differ in terms of near-surface fault geometry, near-surface geological material, surrounding topography and maturity, we assess the %OFD for the two segments separately. Strike-parallel %OFD is 63 ± 34 % for the Sylmar segment and 72 ± 31 % for the Tujunga segment. For the vertical component, average %OFD is larger for the Sylmar segment at 81 ± 22 %, with 55 ± 29 %OFD for the Tujunga segment. The irregularity of %OFD measured in the strike-parallel orientation may reflect the challenges in measuring offsets in the field in an urban environment. On the geometrically simpler, straighter parts of the surface rupture where slip is not distributed onto secondary faults, %OFD in the strike-parallel orientation is still generally higher in the Tujunga segment than the Sylmar segment. Many of the offsets shown in the fault-perpendicular profiles are nonlinear, and have a different shape and width in the three dimensions at the same location, suggesting that different off-fault structures are accommodating different proportions of deformation in the dip slip and strike-slip orientations (Figure 3; Supplementary Figure S2).

In the fault-parallel component, there is little correlation between %OFD and total (profile-derived) offset; however, there is a positive correlation between %OFD and offset in the vertical component (Figure 5A).

4.4 Width of Deformation Zone

In this section we present the average width of the zone of distributed deformation for the main rupture trace (using the ‘preferred’ width measurement), then the averages and standard deviations of the Sylmar and Tujunga segments of the main rupture trace separately. This additional step is taken because the width of diffuse deformation may be affected by attributes that differ between the two segments including near-surface fault geometry, near-surface geological material, surrounding topography and maturity. The average deformation zone width and standard deviations for the main rupture is 101 ± 70 m in the strike-parallel component, and 131 ± 79 m in the vertical component (Figure 4C). Although there is a lot of scatter, the average width of the deformation zone of the strike-parallel component is narrower in the Sylmar segment than the Tujunga segment (87 ± 54 m and 112 ± 82 m respectively). The Sylmar segment has a wider deformation zone on average in the vertical component (143 ± 76 m) compared to the Tujunga segment 120 ± 84 m).

While there is little correlation between %OFD and deformation width (Figure 5B), there is a positive correlation between deformation width and offset (Figure 5C).

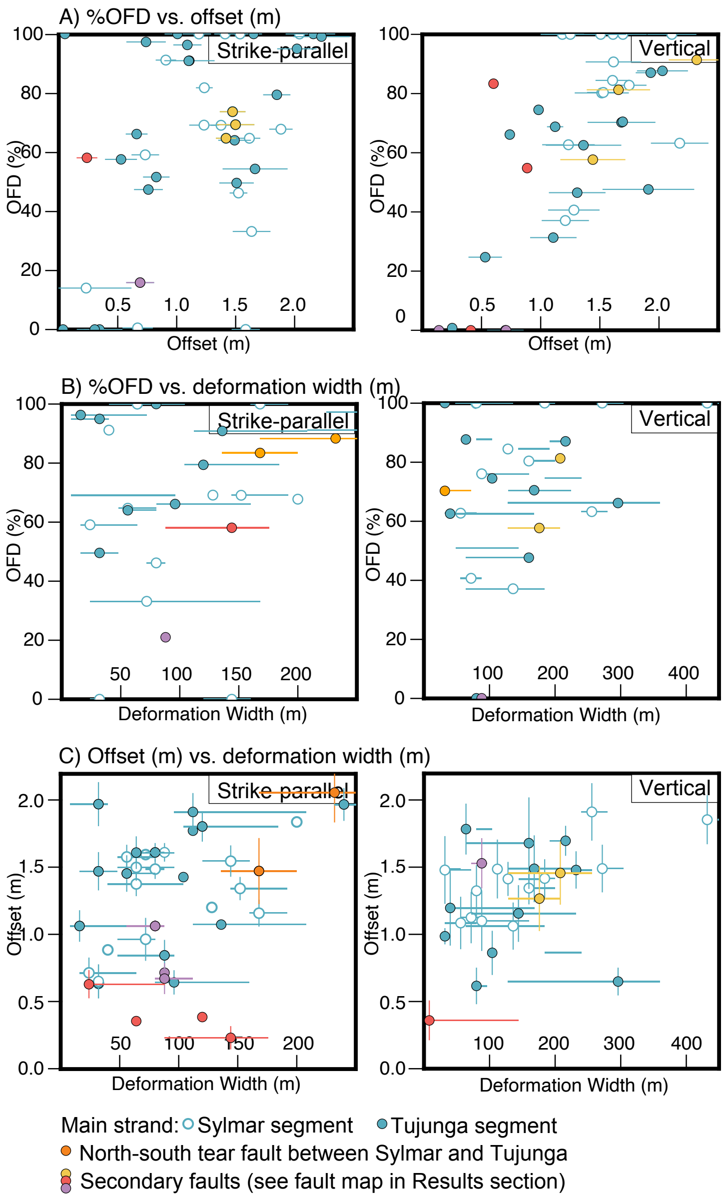

Figure 5. A) Comparison of %OFD and surface offset derived from fault-perpendicular profiles. Colours correspond to fault segments in Figure 1. B) Comparison of %OFD and deformation zone width. C) Comparison of surface offset and deformation zone width.

5 Discussion

We focus here on the vertical and strike-parallel components of deformation, since the striping artifacts in some areas obscure the horizontal shortening component, with particular attention given to the main fault strand.

5.1 Near-Surface Slip Distribution and Rotation of Rake Away From Pre-Stress Direction

Our results are consistent with previous studies in that offset measurements are generally highest and vary more smoothly on simpler, straighter segments of the main fault, and lower and more heterogeneous where there are small wavelength variations in strike and where slip is partitioned onto secondary faults (Figures 2C, 4A; e.g., Klinger et al., 2006; Manighetti et al., 2007; Milliner et al., 2015; Perrin et al., 2016; Bruhat et al., 2020; Ajorlou et al., 2021). This suggests that structural complexity has a primary control on slip distribution.

The roughly equal strike-parallel and vertical surface offsets on the western half of the San Fernando rupture agree with, although are larger than, previously published field and trilateration data (Burford et al., 1971; Meade & Miller, 1973; Morrison, 1973; Savage et al., 1975), and contrast with seismic models that indicate that slip at depth was dominated by thrust faulting (e.g., Langston, 1978; Heaton, 1982). Furthermore, regional stress field estimations are not consistent with the left-lateral surface slip, with the average compression axis oriented 16° from north, approximately perpendicular to the San Fernando fault strike (Stein et al., 1994, and references therein). Dynamic rupture modelling of pure thrust earthquakes reveals a small, temporary component of strike-slip motion induced near the edges of the rupture at shallow depths associated with the passage of the rupture front; however, the dip-slip component still dominates (Hampel et al., 2013; Kearse & Kaneko, 2020). According to these models, the north-dipping San Fernando Fault would see a slight increase in left-lateral slip towards the western rupture termination and a slight increase in right-lateral slip towards the eastern rupture termination. The strike-parallel surface offset pattern of the San Fernando earthquake tells a different story, with left-lateral offset roughly equal to the vertical component in the western half, and on the eastern half, a left-lateral component that decreases towards the eastern termination (Supplementary Figure S3; Barrows et al., 1973; Kahle, 1975).

This asymmetry may be partly due to the oblique (thrust/left-lateral) rake suggested by focal mechanisms determined by P-wave first motions (e.g., Whitcomb et al., 1973); however, the left-lateral component of slip is large enough at the eastern end that there may be an additional factor amplifying the left-lateral motion (Supplementary Figure S3; Barrows et al., 1973). Additionally, Langston (1978); Heaton and Helmberger (1979); Heaton (1982); and Kim (1989) showed that a rupture evolving from oblique slip at depth to pure thrust in the shallower portion of the crust, aligning with the regional stress field (Stein et al., 1994), was more compatible with local and teleseismic data, suggesting that the left-lateral component of slip measured at the surface is too shallow to be resolved using seismic data (Figure 1). Guatteri and Spudich (1998) showed that the local slip direction can change when dynamic stresses radiated from elsewhere on the fault differ from the static prestress. This change is most likely when the prestress is heterogeneous, as expected for ruptures of geometrically-complex, immature faults like in the 1971 San Fernando earthquake (Bouchon, 1978). This can result in a temporal and spatial rotation in rake if the dynamic stresses are amplified enough near the free surface (Guatteri & Spudich, 1998; Oglesby, 2000).

In a surface-rupturing thrust earthquake such as this one, the dipping geometry of the fault amplifies the dynamic stresses in the hanging wall near the free surface and also enhances near-surface slip (Oglesby, 2000). This amplification is consistent with the models proposed by Allen et al. (1998) and Brune (2001) for the San Fernando earthquake, which explain observations such as 1) the intense hanging wall ground shaking that launched a 50 m long piece of asphalt into the air during the earthquake (Maley & Cloud, 1971; Boore, 1972), 2) shattered earth on the hanging wall (Maley & Cloud, 1971; Nason, 1973), and 3) generated the asymmetric static displacements measured by levelling surveys (Burford et al., 1971). The ground motion amplification in the hanging wall of a surfacee-rupturing thrust fault is due to geometric and dynamic effects, such as seismic waves propagating ahead of the rupture reflecting off the free surface and back onto the fault (Oglesby, 2000; Oglesby & Day, 2001b). If the dynamic stresses near the surface did have a different direction than the static prestress, we would expect a temporal rotation in rake due to the high ratio of dynamic to static stress magnitudes until the dynamic stresses wane after the passage of the rupture front resulting in a rotation in rake towards the static prestress direction (Guatteri & Spudich, 1998; Oglesby & Day, 2001a; Kearse & Kaneko, 2020). The temporal rotation in rake is consistent with reports of curved slickenlines found on some 1971 fault plane exposures, including ones near the eastern end of the surface rupture that recorded initial left-lateral slip then a rotation towards the prestress (thrust) slip direction (Kahle, 1975). Nevertheless, we cannot exactly account for the large-left-lateral component.

5.2 Factors Affecting % Off-Fault Deformation

Relatively immature faults are often associated with greater distributed deformation (Dolan & Haravitch, 2014; Milliner et al., 2015; Zinke et al., 2015; Perrin et al., 2016), which is consistent with the generally high %OFD of the San Fernando Fault. However, the distribution of %OFD is different between the vertical and strike-parallel components (Figures 3; 4B): strike-parallel %OFD is 63% in the Sylmar segment, compared to 81% for the vertical component, and in the Tujunga segment, the strike-parallel component's %OFD is 72%, compared to 54% for the vertical component. Near-surface geology may have a primary control over the vertical component of %OFD, with greater average %OFD in the Sylmar segment of the main fault with its thick package of sediments including partially indurated Pliocene-Pleistocene formations (Levi & Yeats, 1993; Langenheim et al., 2011). Fault segment maturity may also play an important role: the lack of hanging wall topography in the Sylmar segment suggests greater immaturity than the Tujunga segment. Vertical %OFD is lower in the more mature Tujunga segment, which cuts through older, stronger and thinner sedimentary rock (Langenheim et al., 2011). Structural complexity may also be a factor in the distribution of %OFD in the vertical component, with generally higher %OFD on the main fault in the presence of subfaults and irregular fault geometry (Figure 4B). Unlike for the vertical component, near-surface geology and segment maturity do not appear to be primary controls in the strike-parallel component, with the Tujunga segment %OFD slightly higher than that of the Sylmar segment (Figure 4B). Moreover, %OFD does not seem to scale with offset magnitude in the fault-parallel component, while there is a positive correlation in the vertical component (Figure 5A).

The partitioning of the vertical and strike-parallel components of %OFD suggests either i) different mechanisms dominated OFD generation in the strike-parallel and vertical components, or ii) an anisotropy in the processes that generated OFD. Of the different mechanisms in play, the short-lived dynamic effects include damage due to seismic waves propagating ahead of the rupture front (Ma, 2008; Thomas & Bhat, 2018) and sudden and short-lived increases in normal stress, shear stress, strain rate, slip rate and rupture velocity around the rupture front (Andrews, 1976; Poliakov et al., 2002; Rice et al., 2005). After the passage of the rupture front, generation of OFD continues at generally lower stresses and strains (Thomas & Bhat, 2018) as slip progresses on the fault, since geometric complexities will locally increase the stress field enough to initiate cracking in the damage zone (Chester & Chester, 2000; Dieterich & Smith, 2009). The previously mentioned temporal rake rotation may explain the different OFD behaviors in the strike-parallel and vertical components. If most of the left-lateral near-surface offset resulted from transient dynamic effects, most of the strike-parallel OFD would have been generated as a result of the high stress and strain rates associated with the passage of the rupture front. While some of the vertical component of OFD would have likely been generated during the very short dynamic stress stage, more OFD will have accumulated as the slip vector rotated towards the prestress (thrust) direction and continued slipping. These very different conditions under which %OFD develops result in different micro- and macrocrack orientations, spatial patterns and magnitudes of %OFD, thus much of the left-lateral and vertical components of OFD likely developed on separate structures, as suggested by the differently shaped offsets of the strike-parallel and vertical displacement profiles (e.g., Figure 3; Supplementary Figure S2; Chester & Chester, 2000; Yamashita, 2000; Templeton & Rice, 2008; Griffith et al., 2010; F. M. Aben et al., 2020). Dynamic rupture models suggest that OFD generated by dynamic stresses is influenced by fault roughness (and therefore fault maturity) and the strength of near-surface materials (Roten et al., 2017; Wollherr et al., 2019). However, the mechanism by which OFD is generated by continued slip on rough surfaces may be more sensitive to fault segment maturity and/or near-surface geology than OFD generated by dynamic stresses, hence the contrast between the Sylmar and Tujunga segments in the vertical component of %OFD that is not replicated in the strike-parallel component. The left-lateral %OFD in the Tujunga segment may have also been enhanced by greater ground motion amplification compared to the Sylmar segment due its much shallower dip and greater hanging wall topography (Boore, 1973; Oglesby, 2000).

Aside from the possibility of different mechanisms generating %OFD in the different components, differences in %OFD in the vertical and strike-parallel orientations could be due to anisotropic OFD mechanisms. For example, preferred orientations of pre-existing off-fault fractures may induce an anisotropy in rock strength that favors dip slip over strike-slip or vice versa (Douglass & Voight, 1969; Peng & Johnson, 1972; Rempe et al., 2013; F. Aben et al., 2016), or the partitioning of OFD onto new structures that accommodate different proportions of dip slip and strike-slip. Moreover, fault roughness has been shown to be anisotropic (Sagy et al., 2007; Candela et al., 2012; Kirkpatrick et al., 2020), which may enhance %OFD in one orientation more than the other, say, if the fault is smoother in the dip-slip orientation than the strike-parallel orientation. The disparity in the vertical but not the horizontal %OFD between the Sylmar and Tujunga segments could also be due to anisotropic fault maturity, where the dip-slip orientation has a more developed damage zone (Scholz, 2019). In other words, the immature Sylmar segment hosts a large amount of OFD because the damage zone may have developed over multiple earthquake cycles but has not yet formed the efficient system of localizing deformation like the Tujunga segment (Scholz, 2019); both fault segments are even more immature in the strike-parallel orientation, hence their moderate and similar %OFD.

5.3 Factors Affecting the Width of Deformation Zone

The poor correlation between %OFD and deformation zone width suggests that these measures have different controls resulting in OFD that can be distributed over different deformation zone widths in different contexts (Figure 5B). For example, the density of off-fault microfractures near the fault core may influence the deformation zone width for a given %OFD. Localized, near-fault offsets are also more irregular than farther-field offsets, affecting the %OFD estimation and introducing some of the scatter into Figure 5B (e.g. Milliner et al., 2015; Scott et al., 2018; Gold et al., 2019, 2021). This is not necessarily representative of the uncertainty, but may also reflect the increase in complexity near the fault core. The Sylmar segment deformation zone measured from the strike-parallel displacement field is generally wider than that of the Tujunga segment, which might mean that in this case, segment maturity or sediment thickness have a primary control on deformation zone width in the strike-parallel orientation, while this does not seem to be the case for %OFD. The wider deformation zone in the vertical orientation may be due to the greater noise level of the DEMs than the optical image correlations, wider deformation caused by progressive slip on the fault, more cumulative slip in the thrust than strike-parallel direction (Mitchell & Faulkner, 2009; Faulkner et al., 2011), or perhaps a reduction in the thrust component of slip near the surface (Gold et al., 2019).

6 Conclusions

Three-dimensional displacement maps of the 1971 San Fernando earthquake from stereo aerial photographs confirm that the component of left-lateral surface offset in this oblique thrust event is higher than expected based on moment tensor inversions and finite fault modelling (e.g., Langston, 1978; Heaton, 1982; Kim, 1989). The rotation of the slip vector may have occurred as a transient dynamic effect based on the amplification of dynamic stresses associated with surface-rupturing thrust faults (Guatteri & Spudich, 1998; Oglesby, 2000), consistent both with the presence of curved slickenlines (Kahle, 1975; Kearse & Kaneko, 2020) and with previous models that attempted to explain the intense ground motions of the San Fernando earthquake (Boore, 1973; Allen et al., 1998). This involves most of the left-lateral slip occurring during the passage of the rupture front, and as these dynamic stresses abate, the slip vector rotating towards the static prestress direction (oblique thrust) as slip progresses on the fault. The generally high %OFD is typical of structurally immature faults, averaging 68% in both the strike-parallel and vertical components. The vertical component of %OFD seems much more sensitive to strength of near-surface geology and/or fault segment maturity compared to the strike-parallel component, which may be due to the different OFD generation mechanisms related to the propagation of the rupture front and progressive fault slip.

Acknowledgments

E. G. was funded through an Alexander Graham Bell Canada Graduate Scholarship and Michael Smith Foreign Study Supplement from NSERC, and a Montalbano Scholars Fellowship and President's Research Scholarship, both from University of Victoria. E. N. was supported by a Canada Research Chair and grants from the Natural Sciences and Engineering Research Council of Canada (NSERC Discovery Grant 2017-04029), the Canada Foundation for Innovation, and the BC Knowledge Development Fund. J.H. was supported by grants from CNES and BQR.

Data Availability Scanned aerial photographs were obtained from the United States Geological Survey's Center for Earth Resources Observation and Science (EROS; http://earthexplorer.usgs.gov). Ames Stereo Pipeline (Beyer et al., 2018) and COSI-Corr (Leprince et al., 2007) were used for data processing. The figures in this paper were generated using Generic Mapping Tools (Wessell et al., 2013). Offsets measured in the field used to calculate off-fault deformation is available through Bonilla et al. (1971); Kamb et al. (1971); Barrows et al. (1973); Sharp (1975) and Supplementary Tables S1 and S2.

References

Aben, F., Doan, M.-L., Mitchell, T., Toussaint, R., Reuschlé, T., Fondriest, M., ... Renard, F. (2016). Dynamic fracturing by successive coseismic loadings leads to pulverization in active fault zones. *Journal of Geophysical Research: Solid Earth*, *121*(4), 2338–2360.

Aben, F. M., Brantut, N., & Mitchell, T. M. (2020). Off-Fault Damage Characterization During and After Experimental Quasi-Static and Dynamic Rupture in Crustal Rock From Laboratory P Wave Tomography and Microstructures. *Journal of Geophysical Research: Solid Earth*, *125*(8), e2020JB019860.

Ajorlou, N., Hollingsworth, J., Mousavi, Z., Ghods, A., & Masoumi, Z. (2021). Characterizing Near-Field Surface Deformation in the 1990 Rudbar Earthquake (Iran) Using Optical Image Correlation. *Geochemistry, Geophysics, Geosystems*, *22*(6), e2021GC009704.

Allen, C. R., Brune, J. N., Cluff, L. S., & Barrows Jr, A. G. (1998). Evidence for unusually strong near-field ground motion on the hanging wall of the San Fernando fault during the 1971 earthquake. *Seismological Research Letters*, *69*(6), 524–531.

Andrews, D. (1976). Rupture velocity of plane strain shear cracks. *Journal of Geophysical Research*, *81*(32), 5679–5687.

Barker, J. S., & Langston, C. A. (1982). Moment tensor inversion of complex earthquakes. *Geophysical Journal International*, *68*(3), 777–803.

Barnhart, W. D., Gold, R. D., Shea, H. N., Peterson, K. E., Briggs, R. W., & Harbor, D. J. (2019). Vertical Coseismic Offsets Derived From High-Resolution Stereogrammetric DSM Differencing: The 2013 Baluchistan, Pakistan Earthquake. *Journal of Geophysical Research (Solid Earth)*, *124*(6), 6039-6055. doi: 10.1029/2018JB017107

Barrows, A. G. (1975). Surface Effects and Related Geology of the San Fernando Earthquake in the Foothill Region Between Little Tujunga and Wilson Canyons. In G. Oakeshott (Ed.), *San Fernando Earthquake of 9 February 1971* (Vol. 196, pp. 97–117). Sacramento, CA: California Division of Mines and Geology.

Barrows, A. G., Kahle, J. E., Weber, F. H., & Saul, R. (1973). Map of surface breaks resulting from the San Fernando, California, earthquake. In L. Murphy (Ed.), *San Fernando, California, Earthquake of February 9, 1971* (Vol. 3, pp. 127 – 134). Washington, D.C., USA: U.S. Department of Commerce, National Oceanic and Atmospheric Administration.

Barrows, A. G., Kahle, J. E., Weber, F. H., Saul, R., & Morton, D. (1975). Surface Effects Map of the San Fernando Earthquake Area (scale 1:24,000). In G. Oakeshott (Ed.), *San Fernando Earthquake of 9 February 1971* (Vol. 196, p. Plate 3). Sacramento, CA: California Division of Mines and Geology.

Ben-Zion, Y., & Sammis, C. G. (2003). Characterization of Fault Zones. *Pure and Applied Geophysics*, *160*(3-4), 677-715. doi: 10.1007/PL00012554

Beyer, R. A., Alexandrov, O., & McMichael, S. (2018). The Ames Stereo Pipeline: NASA's open source software for deriving and processing terrain data. *Earth and Space Science*, *5*(9), 537–548.

Bonilla, M. (1973). Trench Exposures Across Surface Fault Ruptures Associated With San Fernando Earthquake. In L. Murphy (Ed.), *San Fernando, California, Earthquake of February 9, 1971* (Vol. 3, pp. 173 – 182). Washington, D.C., USA: U.S. Department of Commerce, National Oceanic and Atmospheric Administration.

Bonilla, M. G., Buchanan, J. M., Castle, R. ., Clark, M. M., Frizzell, V. A., Gulliver, R. M., . . . I., Z. J. (1971). Surface Faulting. In *The San Fernando, California Earthquake of February 9th, 1971* (pp. 56 – 76). Washington, D.C., USA: U.S. Geological Survey.

Boore, D. M. (1972). A note on the effect of simple topography on seismic SH waves. *Bulletin of the Seismological Society of America*, *62*(1), 275–284.

Boore, D. M. (1973). The effect of simple topography on seismic waves: implications for the accelerations recorded at Pacoima Dam, San Fernando Valley, California. *Bulletin of the seismological society of America*, *63*(5), 1603–1609.

Bouchon, M. (1978). A dynamic source model for the San Fernando earthquake. *Bulletin of the Seismological Society of America*, *68*(6), 1555–1576.

Bruhat, L., Fang, Z., & Dunham, E. M. (2016). Rupture complexity and the supershear transition on rough faults. *Journal of Geophysical Research: Solid Earth*, *121*(1), 210–224.

Bruhat, L., Klinger, Y., Vallage, A., & Dunham, E. M. (2020). Influence of fault roughness on surface displacement: from numerical simulations to coseismic

slip distributions. *Geophysical Journal International*, *220*(3), 1857–1877.
Brune, J. N. (2001). Shattered rock and precarious rock evidence for strong asymmetry in ground motions during thrust faulting. *Bulletin of the Seismological Society of America*, *91*(3), 441–447.
Burford, R., Castle, R., Church, J., Kinoshita, S., Kirby, S., Ruthven, R., & Savage, J. (1971). Preliminary measurements of tectonic movement. In *The San Fernando, California Earthquake of February 9th, 1971* (pp. 80 – 85). Washington, D.C., USA: U.S. Geological Survey.
Bürgmann, R., Pollard, D. D., & Martel, S. J. (1994). Slip distributions on faults: effects of stress gradients, inelastic deformation, heterogeneous host-rock stiffness, and fault interaction. *Journal of Structural Geology*, *16*(12), 1675-1690. doi: 10.1016/0191-8141(94)90134-1
Candela, T., Renard, F., Klinger, Y., Mair, K., Schmittbuhl, J., & Brodsky, E. E. (2012). Roughness of fault surfaces over nine decades of length scales. *Journal of Geophysical Research (Solid Earth)*, *117*(B8), B08409. doi: 10.1029/2011JB009041
Carena, S., & Suppe, J. (2002). Three-dimensional imaging of active structures using earthquake aftershocks: the Northridge thrust, California. *Journal of Structural Geology*, *24*(4), 887-904. doi: 10.1016/S0191-8141(01)00110-9
Cheng, G., & Barnhart, W. D. (2021). Permanent co-seismic deformation of the 2013 Mw7. 7 Baluchistan, Pakistan earthquake from high-resolution surface strain analysis. *Journal of Geophysical Research: Solid Earth*, *126*(3), e2020JB020622.
Chester, F. M., & Chester, J. S. (2000). Stress and deformation along wavy frictional faults. *Journal of Geophysical Research: Solid Earth*, *105*(B10), 23421–23430.
Cochran, E. S., Li, Y. G., Shearer, P. M., Barbot, S., Fialko, Y., & Vidale, J. E. (2009). Seismic and geodetic evidence for extensive, long-lived fault damage zones. *Geology*, *37*(4), 315-318. doi: 10.1130/G25306A.1
Dieterich, J. H., & Smith, D. E. (2009). Nonplanar faults: Mechanics of slip and off-fault damage. In *Mechanics, structure and evolution of fault zones* (pp. 1799–1815). Springer.
Dolan, J. F., & Haravitch, B. D. (2014). How well do surface slip measurements track slip at depth in large strike-slip earthquakes? The importance of fault structural maturity in controlling on-fault slip versus off-fault surface deformation. *Earth and Planetary Science Letters*, *388*, 38-47. doi: 10.1016/j.epsl.2013.11.043
Douglass, P. M., & Voight, B. (1969). Anisotropy of granites: a reflection of microscopic fabric. *Geotechnique*, *19*(3), 376–398.
Faulkner, D., Mitchell, T., Jensen, E., & Cembrano, J. (2011). Scaling of fault damage zones with displacement and the implications for fault growth processes. *Journal of Geophysical Research: Solid Earth*, *116*(B5).
Fialko, Y., Sandwell, D., Agnew, D., Simons, M., Shearer, P., & Minster, B. (2002). Deformation on Nearby Faults Induced by the 1999 Hector Mine Earthquake. *Science*, *297*(5588), 1858-1862. doi: 10.1126/science.1074671
Fialko, Y., Sandwell, D., Simons, M., & Rosen, P. (2005). Three-dimensional deformation caused by the bam, iran, earthquake and the origin of shallow slip deficit. *Nature*, *435*(7040), 295–299.
Fuis, G. S., Clayton, R. W., Davis, P. M., Ryberg, T., Lutter, W. J., Okaya, D. A., ... Keller, G. R. (2003). Fault systems of the 1971 San Fernando and 1994 Northridge earthquakes, southern California: Relocated aftershocks and seismic images from LARSE II. *Geology*, *31*(2), 171. doi: 10.1130/0091-7613(2003)031⟨0171:FSOTSF⟩2.0.CO;2
Gaudreau, É., Nissen, E. K., Bergman, E. A., Benz, H. M., Tan, F., & Karasözen, E. (2019). The August 2018 Kaktovik Earthquakes: Active Tectonics in North-

eastern Alaska Revealed With InSAR and Seismology. *Geophysical Research Letters*, *46*(24), 14,412-14,420. doi: 10.1029/2019GL085651

Gold, R. D., Clark, D., Barnhart, W. D., King, T., Quigley, M., & Briggs, R. W. (2019). Surface Rupture and Distributed Deformation Revealed by Optical Satellite Imagery: The Intraplate 2016 M_w 6.0 Petermann Ranges Earthquake, Australia. *Geophysical Research Letters*, *46*(10394), 10,394-10,403. doi: 10.1029/2019GL084926

Gold, R. D., DuRoss, C. B., & Barnhart, W. D. (2021). Coseismic Surface Displacement in the 2019 Ridgecrest Earthquakes: Comparison of Field Measurements and Optical Image Correlation Results. *Geochemistry, Geophysics, Geosystems*, *22*(3), e09326. doi: 10.1029/2020GC009326

Griffith, W. A., Nielsen, S., Di Toro, G., & Smith, S. A. (2010). Rough faults, distributed weakening, and off-fault deformation. *Journal of Geophysical Research: Solid Earth*, *115*(B8).

Guatteri, M., & Spudich, P. (1998). Coseismic temporal changes of slip direction: the effect of absolute stress on dynamic rupture. *Bulletin of the Seismological Society of America*, *88*(3), 777–789.

Hampel, A., Li, T., & Maniatis, G. (2013). Contrasting strike-slip motions on thrust and normal faults: Implications for space-geodetic monitoring of surface deformation. *Geology*, *41*(3), 299-302. doi: 10.1130/G33927.1

Harrington, R. M., & Brodsky, E. E. (2009). Source duration scales with magnitude differently for earthquakes on the San Andreas Fault and on secondary faults in Parkfield, California. *Bulletin of the Seismological Society of America*, *99*(4), 2323–2334.

Heaton, T. H. (1982). The 1971 San Fernando earthquake: A double event? *Bulletin of the Seismological Society of America*, *72*(6A), 2037–2062.

Heaton, T. H., & Helmberger, D. V. (1979). Generalized ray models of the San Fernando earthquake. *Bulletin of the Seismological Society of America*, *69*(5), 1311–1341.

Huang, Y. (2018). Earthquake rupture in fault zones with along-strike material heterogeneity. *Journal of Geophysical Research: Solid Earth*, *123*(11), 9884–9898.

Jackson, J., Bouchon, M., Fielding, E., Funning, G., Ghorashi, M., Hatzfeld, D., … others (2006). Seismotectonic, rupture process, and earthquake-hazard aspects of the 2003 December 26 Bam, Iran, earthquake. *Geophysical Journal International*, *166*(3), 1270–1292.

Jara, J., Bruhat, L., Thomas, M. Y., Antoine, S. L., Okubo, K., Rougier, E., … others (2021). Signature of transition to supershear rupture speed in the coseismic off-fault damage zone. *Proceedings of the Royal Society A*, *477*(2255), 20210364.

Kahle, J. E. (1975). Surface Effects and Related Geology of the Lakeview Fault Segment of the San Fernando Fault Zone. In G. Oakeshott (Ed.), *San Fernando Earthquake of 9 February 1971* (Vol. 196, pp. 119–135). Sacramento, CA: California Division of Mines and Geology.

Kamb, B., Silver, L., Abrams, L., Carter, B., Jordan, T., & Minster, J. (1971). Pattern of faulting and nature of fault movement in the San Fernando earthquake. In *The San Fernando, California Earthquake of February 9th, 1971* (pp. 41 – 55). Washington, D.C., USA: U.S. Geological Survey.

Kaneko, Y., & Fialko, Y. (2011). Shallow slip deficit due to large strike-slip earthquakes in dynamic rupture simulations with elasto-plastic off-fault response. *Geophysical Journal International*, *186*(3), 1389–1403.

Kearse, J., & Kaneko, Y. (2020). On-Fault Geological Fingerprint of Earthquake Rupture Direction. *Journal of Geophysical Research (Solid Earth)*, *125*(9), e19863. doi: 10.1029/2020JB019863

Kim, J. (1989). *Complex seismic sources and time-dependent moment tensor inversion* (Unpublished doctoral dissertation). University of Arizona.

Kirkpatrick, J. D., Edwards, J. H., Verdecchia, A., Kluesner, J. W., Harrington, R. M., & Silver, E. A. (2020). Subduction megathrust heterogeneity characterized from 3D seismic data. *Nature Geoscience*, *13*(5), 369–374.

Klinger, Y., Michel, R., & King, G. (2006). Evidence for an earthquake barrier model from Mw 7.8 Kokoxili (Tibet) earthquake slip-distribution. *Earth and Planetary Science Letters*, *242*(3-4), 354–364.

Langenheim, V. E., Wright, T. L., Okaya, D. A., Yeats, R. S., Fuis, G. S., Thygesen, K., & Thybo, H. (2011). Structure of the San Fernando Valley region, California: Implications for seismic hazard and tectonic history. *Geosphere*, *7*(2), 528-572. doi: 10.1130/GES00597.1

Langston, C. A. (1978). The February 9, 1971 San Fernando earthquake: a study of source finiteness in teleseismic body waves. *Bulletin of the Seismological Society of America*, *68*(1), 1–29.

Leprince, S., Barbot, S., Ayoub, F., & Avouac, J.-P. (2007). Automatic and Precise Orthorectification, Coregistration, and Subpixel Correlation of Satellite Images, Application to Ground Deformation Measurements. *IEEE Transactions on Geoscience and Remote Sensing*, *45*, 1529-1558. doi: 10.1109/TGRS.2006.888937

Levi, S., & Yeats, R. S. (1993). Paleomagnetic constraints on the initiation of uplift on the Santa Susana Fault, Western Transverse Ranges, California. *Tectonics*, *12*(3), 688-702. doi: 10.1029/93TC00133

Lockner, D., Byerlee, J., Kuksenko, V., Ponomarev, A., & Sidorin, A. (1991). Quasi-static fault growth and shear fracture energy in granite. *Nature*, *350*(6313), 39–42.

Lyakhovsky, V., Ben-Zion, Y., & Agnon, A. (1997). Distributed damage, faulting, and friction. *Journal of Geophysical Research: Solid Earth*, *102*(B12), 27635–27649.

Ma, S. (2008). A physical model for widespread near-surface and fault zone damage induced by earthquakes. *Geochemistry, Geophysics, Geosystems*, *9*(11), Q11009. doi: 10.1029/2008GC002231

Maley, R., & Cloud, W. (1971). Preliminary strong-motion results from the San Fernando earthquake of February 9, 1971. In *The San Fernando, California Earthquake of February 9th, 1971* (pp. 163 – 176). Washington, D.C., USA: U.S. Geological Survey.

Manighetti, I., Campillo, M., Bouley, S., & Cotton, F. (2007). Earthquake scaling, fault segmentation, and structural maturity. *Earth and Planetary Science Letters*, *253*(3-4), 429-438. doi: 10.1016/j.epsl.2006.11.004

Martel, S. J., Pollard, D. D., & Segall, P. (1988). Development of simple strike-slip fault zones, Mount Abbot quadrangle, Sierra Nevada, California. *Geological Society of America Bulletin*, *100*(9), 1451–1465.

Meade, B. K., & Miller, R. W. (1973). Horizontal Crustal Movements Determined From Surveys After San Fernando Earthquake. In L. Murphy (Ed.), *San Fernando, California, Earthquake of February 9, 1971* (Vol. 3, pp. 243 – 293). Washington, D.C., USA: U.S. Department of Commerce, National Oceanic and Atmospheric Administration.

Milliner, C., Donnellan, A., Aati, S., Avouac, J.-P., Zinke, R., Dolan, J. F., ... Bürgmann, R. (2021). Bookshelf Kinematics and the Effect of Dilatation on Fault Zone Inelastic Deformation: Examples From Optical Image Correlation Measurements of the 2019 Ridgecrest Earthquake Sequence. *Journal of Geophysical Research: Solid Earth*, *126*(3), e2020JB020551.

Milliner, C. W. D., Dolan, J. F., Hollingsworth, J., Leprince, S., Ayoub, F., & Sammis, C. G. (2015). Quantifying near-field and off-fault deformation patterns of the 1992 M_w 7.3 Landers earthquake. *Geochemistry, Geophysics, Geosystems*, *16*(5), 1577-1598. doi: 10.1002/2014GC005693

Mitchell, T., & Faulkner, D. (2009). The nature and origin of off-fault damage surrounding strike-slip fault zones with a wide range of displacements: A field study from the Atacama fault system, northern Chile. *Journal of Structural Geology*, *31*(8), 802–816.

Mori, J., Wald, D. J., & Wesson, R. L. (1995). Overlapping fault planes of the 1971 San Fernando and 1994 Northridge, California earthquakes. *Geophysical Research Letters*, *22*(9), 1033-1036. doi: 10.1029/95GL00712

Morrison, N. L. (1973). Vertical Crustal Movements Determined From Surveys Before and After San Fernando Earthquake. In L. Murphy (Ed.), *San Fernando, California, Earthquake of February 9, 1971* (Vol. 3, pp. 295 – 324). Washington, D.C., USA: U.S. Department of Commerce, National Oceanic and Atmospheric Administration.

Nason, R. D. (1973). Increased seismic shaking above a thrust fault. In G. Oakeshott, N. A. Benfer, J. L. Coffman, J. R. Bernick, & L. T. Dees (Eds.), *San Fernando, California, Earthquake of 9, February 1971* (Vol. 3, pp. 123–126). Washington, DC: U.S. Department of Commerce.

Oglesby, D. D. (2000). The Three-Dimensional Dynamics of Dipping Faults. *The Bulletin of the Seismological Society of America*, *90*(3), 616-628. doi: 10.1785/0119990113

Oglesby, D. D., & Day, S. M. (2001a). The effect of fault geometry on the 1999 Chi-Chi (Taiwan) earthquake. *Geophysical Research Letters*, *28*(9), 1831–1834.

Oglesby, D. D., & Day, S. M. (2001b). Fault geometry and the dynamics of the 1999 Chi-Chi (Taiwan) earthquake. *Bulletin of the Seismological Society of America*, *91*(5), 1099–1111.

Oskin, M. E., Arrowsmith, J. R., Corona, A. H., Elliott, A. J., Fletcher, J. M., Fielding, E. J., ... others (2012). Near-field deformation from the El Mayor–Cucapah earthquake revealed by differential LIDAR. *Science*, *335*(6069), 702–705.

Peng, S., & Johnson, A. (1972). Crack growth and faulting in cylindrical specimens of Chelmsford granite. *International Journal of Rock Mechanics and Mining Sciences*, *9*(1), 37–86.

Perrin, C., Manighetti, I., Ampuero, J.-P., Cappa, F., & Gaudemer, Y. (2016). Location of largest earthquake slip and fast rupture controlled by along-strike change in fault structural maturity due to fault growth. *Journal of Geophysical Research: Solid Earth*, *121*(5), 3666–3685.

Poliakov, A. N., Dmowska, R., & Rice, J. R. (2002). Dynamic shear rupture interactions with fault bends and off-axis secondary faulting. *Journal of Geophysical Research: Solid Earth*, *107*(B11), ESE–6.

Pousse-Beltran, L., Nissen, E., Bergman, E. A., Cambaz, M. D., Gaudreau, É., Karasözen, E., & Tan, F. (2020). The 2020 Mw 6.8 Elazığ (Turkey) earthquake reveals rupture behavior of the East Anatolian Fault. *Geophysical Research Letters*, *47*(13), e2020GL088136.

Proctor, R., Crook, J., R., McKeown, M., & Moresco, R. (1972). Relation of known faults to surface ruptures, 1971 San Fernando earthquake, southern California. *Geological Society of America Bulletin*, *83*, 1601–1618.

Quigley, M., Van Dissen, R., Litchfield, N., Villamor, P., Duffy, B., Barrell, D., ... Noble, D. (2012). Surface rupture during the 2010 Mw 7.1 Darfield (Canterbury) earthquake: Implications for fault rupture dynamics and seismic-hazard analysis. *Geology*, *40*(1), 55–58.

Radiguet, M., Cotton, F., Manighetti, I., Campillo, M., & Douglas, J. (2009). Dependency of Near-Field Ground Motions on the Structural Maturity of the Ruptured Faults. *The Bulletin of the Seismological Society of America*, *99*(4), 2572-2581. doi: 10.1785/0120080340

Rempe, M., Mitchell, T., Renner, J., Nippress, S., Ben-Zion, Y., & Rockwell, T. (2013). Damage and seismic velocity structure of pulverized rocks near the San Andreas Fault. *Journal of Geophysical Research: Solid Earth*, *118*(6),

2813–2831.
Rice, J. R., Sammis, C. G., & Parsons, R. (2005). Off-fault secondary failure induced by a dynamic slip pulse. *Bulletin of the Seismological Society of America*, *95*(1), 109–134.
Roten, D., Olsen, K., & Day, S. (2017). Off-fault deformations and shallow slip deficit from dynamic rupture simulations with fault zone plasticity. *Geophysical Research Letters*, *44*(15), 7733–7742.
Sagy, A., Brodsky, E. E., & Axen, G. J. (2007). Evolution of fault-surface roughness with slip. *Geology*, *35*(3), 283. doi: 10.1130/G23235A.1
Savage, J., Burford, R., & Kinoshita, W. (1975). Earth movements from geodetic measurements. In G. Oakeshott (Ed.), *San Fernando Earthquake of 9 February 1971* (Vol. 196, pp. 175 – 186). Sacramento, CA: California Division of Mines and Geology.
Scholz, C. H. (2019). *The Mechanics of Earthquakes and Faulting* (3rd ed.). Cambridge, UK: Cambridge University Press.
Scott, C. P., Arrowsmith, J. R., Nissen, E., Lajoie, L., Maruyama, T., & Chiba, T. (2018). The M7 2016 Kumamoto, Japan, earthquake: 3-D deformation along the fault and within the damage zone constrained from differential lidar topography. *Journal of Geophysical Research: Solid Earth*, *123*(7), 6138–6155.
Sharp, R. V. (1975). Displacement on tectonic ruptures. In G. Oakeshott (Ed.), *San Fernando Earthquake of 9 February 1971* (Vol. 196, pp. 187–194). Sacramento, CA: California Division of Mines and Geology.
Stein, R. S., King, G. C., & Lin, J. (1994). Stress triggering of the 1994 M= 6.7 Northridge, California, earthquake by its predecessors. *Science*, *265*(5177), 1432–1435.
Templeton, E. L., & Rice, J. R. (2008). Off-fault plasticity and earthquake rupture dynamics: 1. Dry materials or neglect of fluid pressure changes. *Journal of Geophysical Research: Solid Earth*, *113*(B9).
Thakur, P., Huang, Y., & Kaneko, Y. (2020). Effects of Low-Velocity Fault Damage Zones on Long-Term Earthquake Behaviors on Mature Strike-Slip Faults. *Journal of Geophysical Research (Solid Earth)*, *125*(8), e19587. doi: 10.1029/2020JB019587
Thomas, M. Y., & Bhat, H. S. (2018). Dynamic evolution of off-fault medium during an earthquake: a micromechanics based model. *Geophysical Journal International*, *214*(2), 1267–1280.
Thomas, M.Y. and Bhat, H.S. and Klinger, Y. (2017). Effect of brittle off-fault damage on earthquake rupture dynamics. In M. Thomas, H. Bhat, & T. Mitchell (Eds.), *Fault zone dynamic processes: Evolution of fault properties during seismic rupture* (Vol. 227, pp. 255 – 280). Washington, DC: American Geophysical Union. doi: https://doi.org/10.1002/9781119156895.ch14
Townley, S. D., & Allen, M. W. (1939). Descriptive catalog of earthquakes of the Pacific Coast of the United States 1769 to 1928. *Bulletin of the Seismological Society of America*, *29*(1), 1–297.
Tsutsumi, H., & Yeats, R. S. (1999). Tectonic setting of the 1971 Sylmar and 1994 Northridge earthquakes in the San Fernando Valley, California. *Bulletin of the Seismological Society of America*, *89*(5), 1232–1249.
Weber, F. H. (1975). Surface effects and related geology of the San Fernando earthquake in the Sylmar area. In G. Oakeshott (Ed.), *San Fernando Earthquake of 9 February 1971* (Vol. 196, pp. 71–96). Sacramento, CA: California Division of Mines and Geology.
Wentworth, C. M., Yerkes, R., & Allen, C. R. (1971). Geologic setting and activity of faults in the San Fernando area, California. In *The San Fernando, California Earthquake of February 9th, 1971* (pp. 6 – 16). Washington, D.C., USA: U.S. Geological Survey.
Wesnousky, S. G. (1988). Seismological and structural evolution of strike-slip faults.

Nature, *335* (6188), 340–343.
Wesnousky, S. G. (1990). Seismicity as a function of cumulative geologic offset: some observations from southern California. *Bulletin of the Seismological Society of America*, *80* (5), 1374–1381.
Wessell, P., Smith, W., Scharroo, R., Luis, J., & Wobbe, F. (2013). Generic Mapping Tools: Improved Version Released. *Eos Transactions*, *94*, 409–410.
Whitcomb, J. H., Allen, C. R., Garmany, J. D., & Hileman, J. A. (1973). San Fernando earthquake series, 1971: focal mechanisms and tectonics. *Reviews of Geophysics*, *11* (3), 693–730.
Wollherr, S., Gabriel, A.-A., & Mai, P. M. (2019). Landers 1992 "reloaded": Integrative dynamic earthquake rupture modeling. *Journal of Geophysical Research: Solid Earth*, *124* (7), 6666–6702.
Xu, X., Tong, X., Sandwell, D. T., Milliner, C. W., Dolan, J. F., Hollingsworth, J., … Ayoub, F. (2016). Refining the shallow slip deficit. *Geophysical Journal International*, *204* (3), 1867–1886.
Yamashita, T. (2000). Generation of microcracks by dynamic shear rupture and its effects on rupture growth and elastic wave radiation. *Geophysical Journal International*, *143* (2), 395–406.
Zinke, R., Dolan, J. F., Van Dissen, R., Grenader, J. R., Rhodes, E. J., McGuire, C. P., … Hatem, A. E. (2015). Evolution and progressive geomorphic manifestation of surface faulting: A comparison of the Wairau and Awatere faults, South Island, New Zealand. *Geology*, *43* (11), 1019–1022.
Zinke, R., Hollingsworth, J., & Dolan, J. F. (2014). Surface slip and off-fault deformation patterns in the 2013 M_w 7.7 Balochistan, Pakistan earthquake: Implications for controls on the distribution of near-surface coseismic slip. *Geochemistry, Geophysics, Geosystems*, *15* (12), 5034-5050. doi: 10.1002/2014GC005538
Zinke, R., Hollingsworth, J., Dolan, J. F., & Van Dissen, R. (2019). Three-Dimensional Surface Deformation in the 2016 M_W 7.8 Kaikōura, New Zealand, Earthquake From Optical Image Correlation: Implications for Strain Localization and Long-Term Evolution of the Pacific-Australian Plate Boundary. *Geochemistry, Geophysics, Geosystems*, *20* (3), 1609-1628. doi: 10.1029/2018GC007951

Figure 1.

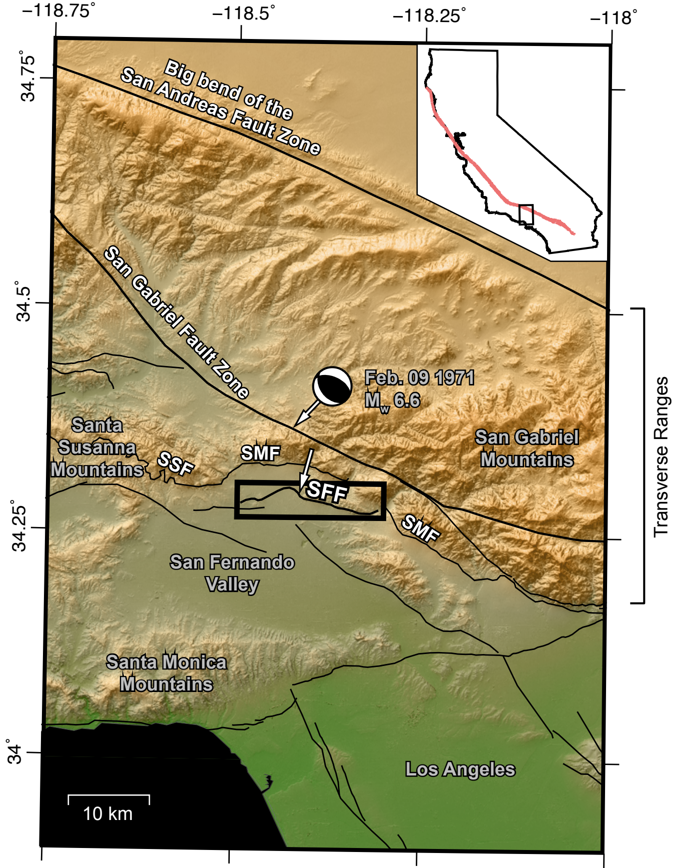

−118.75°
−118.5°
−118.25°
−118°
34.75°
34.5°
34.25°
34°
Big bend of the
San Andreas Fault Zone
San Gabriel Fault Zone
Feb. 09 1971
M_w 6.6
Santa
Susanna
Mountains
SSF
SMF
SFF
SMF
San Gabriel
Mountains
Transverse Ranges
San Fernando
Valley
Santa Monica
Mountains
Los Angeles
10 km

Figure 2.

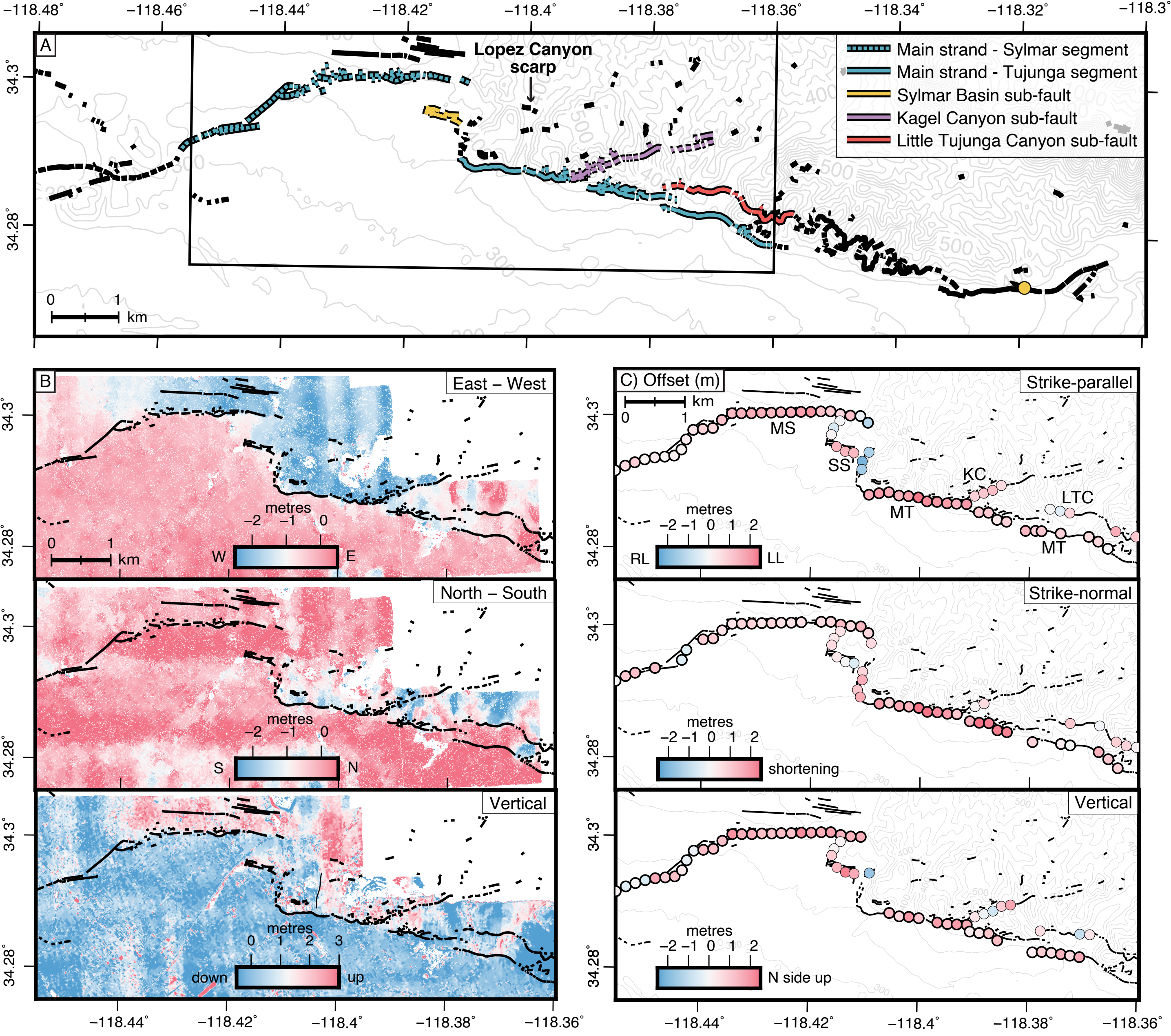

A
Lopez Canyon scarp
Main strand - Sylmar segment
Main strand - Tujunga segment
Sylmar Basin sub-fault
Kagel Canyon sub-fault
Little Tujunga Canyon sub-fault
0 1 km
B
East – West
metres
−2 −1 0
W E
North – South
S N
Vertical
0 1 2 3
down up
C) Offset (m)
Strike-parallel
MS
SS
MT
KC
LTC
−2 −1 0 1 2
RL LL
Strike-normal
shortening
N side up
−118.48° −118.46° −118.44° −118.42° −118.4° −118.38° −118.36° −118.34° −118.32°
34.3° 34.28°

Figure 3.

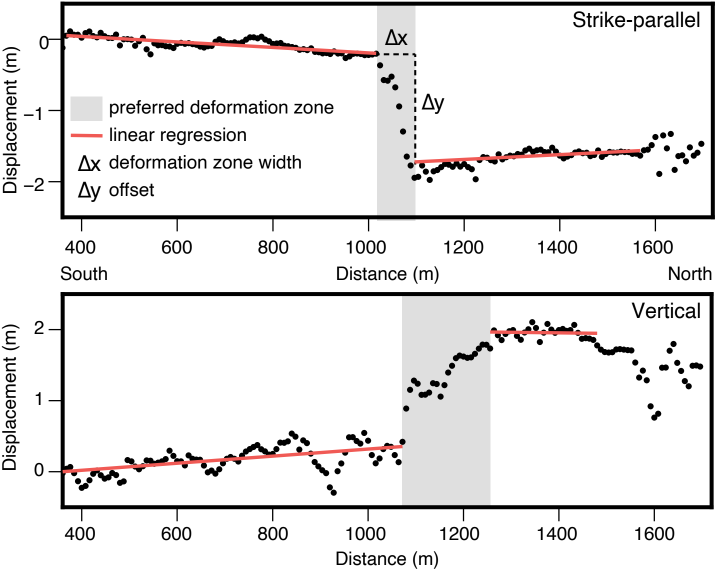
Strike-parallel
Δx
Δy
preferred deformation zone
linear regression
Δx deformation zone width
Δy offset
Displacement (m)
0
−1
−2
400
600
800
1000
1200
1400
1600
South
Distance (m)
North
Vertical
Displacement (m)
2
1
0
400
600
800
1000
1200
1400
1600
Distance (m)

Figure 4.

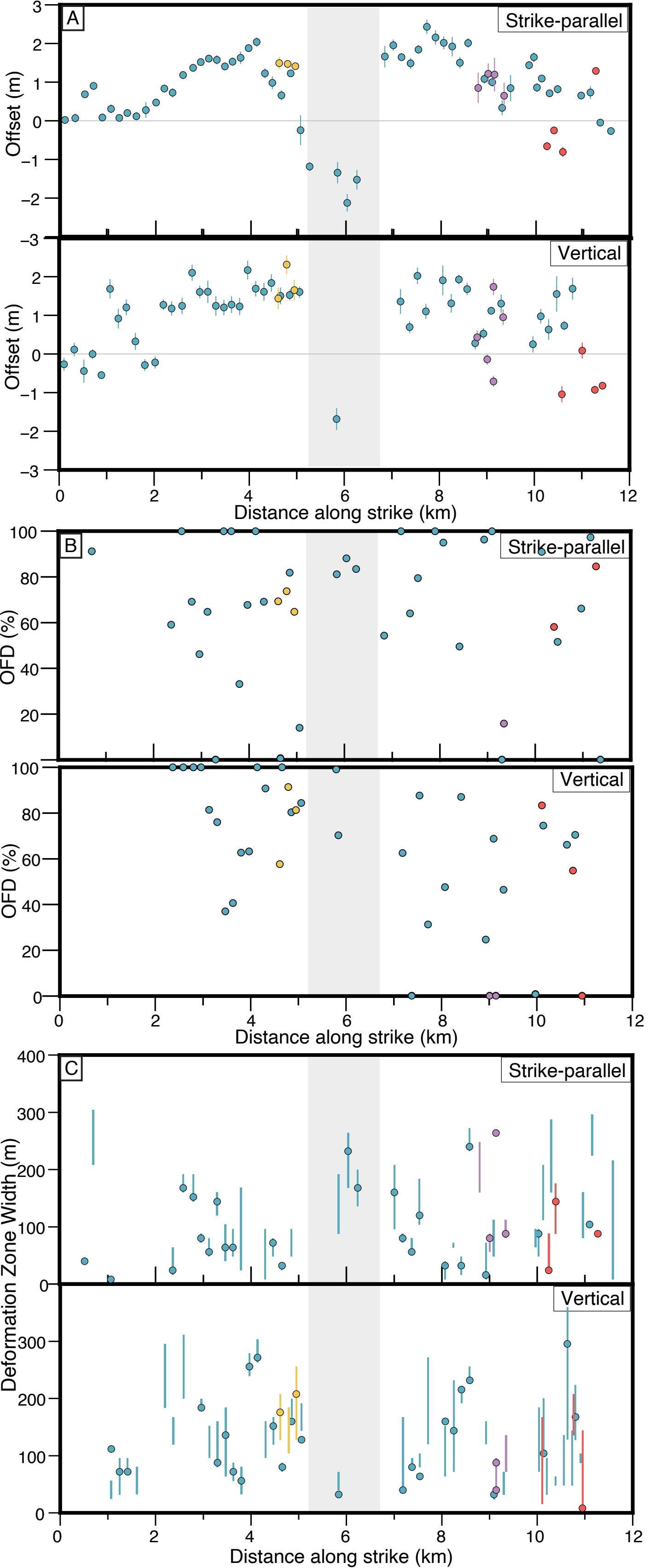
A
Strike-parallel
Vertical
Offset (m)
Distance along strike (km)
B
OFD (%)
C
Deformation Zone Width (m)

Figure 5.

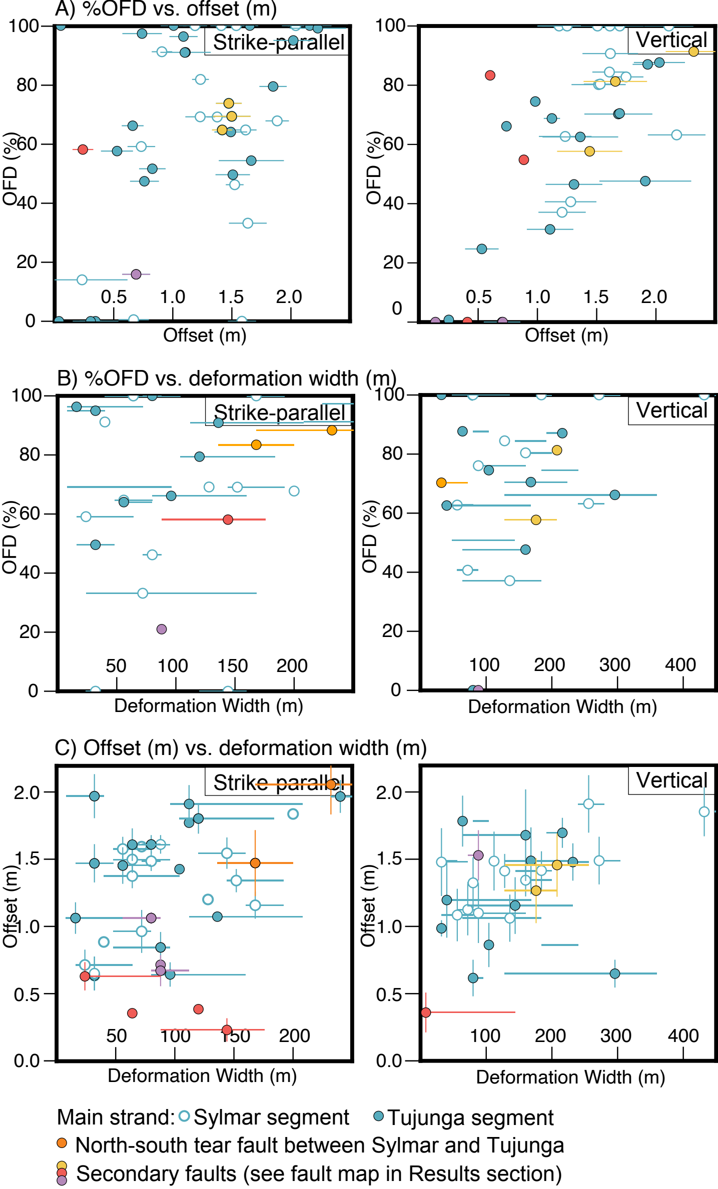
A) %OFD vs. offset (m)
Strike-parallel
Vertical
OFD (%)
Offset (m)
B) %OFD vs. deformation width (m)
Strike-parallel
Vertical
OFD (%)
Deformation Width (m)
C) Offset (m) vs. deformation width (m)
Strike-parallel
Vertical
Offset (m)
Deformation Width (m)
Main strand: Sylmar segment
Tujunga segment
North-south tear fault between Sylmar and Tujunga
Secondary faults (see fault map in Results section)

Supporting Information for "Complex 3-D surface deformation in the 1971 San Fernando, California earthquake reveals static and dynamic controls on off-fault deformation"

É. Gaudreau[1], J. Hollingsworth[2], E. Nissen[1], G. Funning[3]

[1]University of Victoria, Victoria, Canada

[2]ISTerre, Université Grenoble-Alpes, Grenoble, France

[3]University of California Riverside, Riverside, USA

Contents of this file

1. Figures S1 to S3
2. Tables S1 to S3

Additional Supporting Information (Files uploaded separately)

1. Table S1. Strike-parallel offsets, field measurements used in OFD estimation and OFD from strike-perpendicular profiles. Some field measurements have been projected to be perpendicular to each profile. Fault ID corresponds to the different fault segments mentioned in the text: MS: main rupture strand – Sylmar segment. MT: main strand – Tujunga segment. SS: Sylmar secondary fault. KS: Kagel Canyon secondary fault. TS: Little Tujunga Canyon secondary fault.

2. Table S2. Vertical offsets, field measurements used in OFD estimation and OFD from strike-perpendicular profiles. See Table S1 for fault ID explanation.

Introduction

The supporting information provides more information on the full 3-D displacement field, strike-perpendicular profiles used to measure offsets, fault zone deformation and fault zone widths.

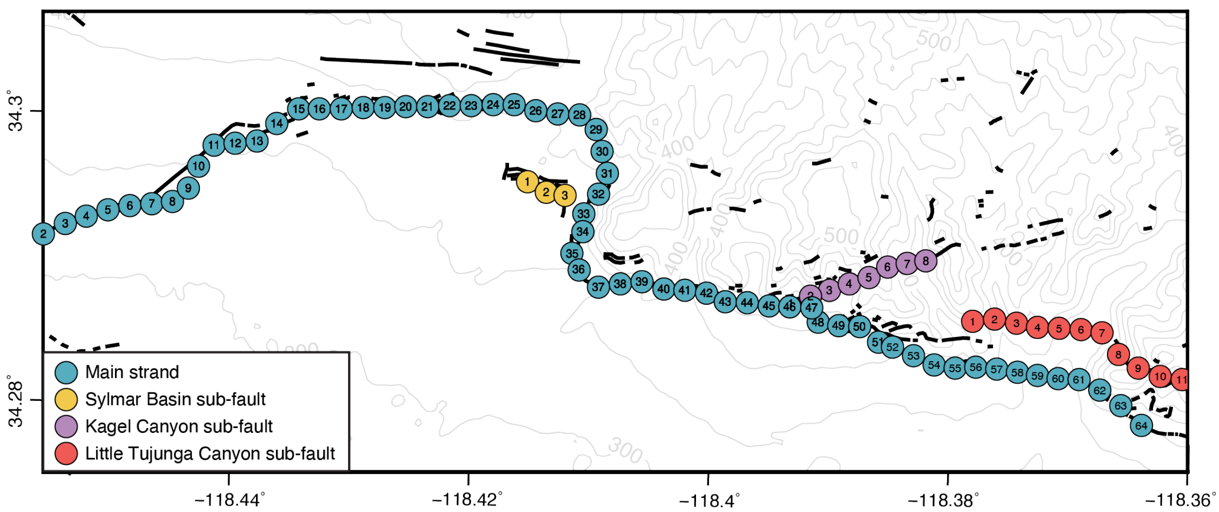

Figure S1. Map showing location of profiles in Figure S2.

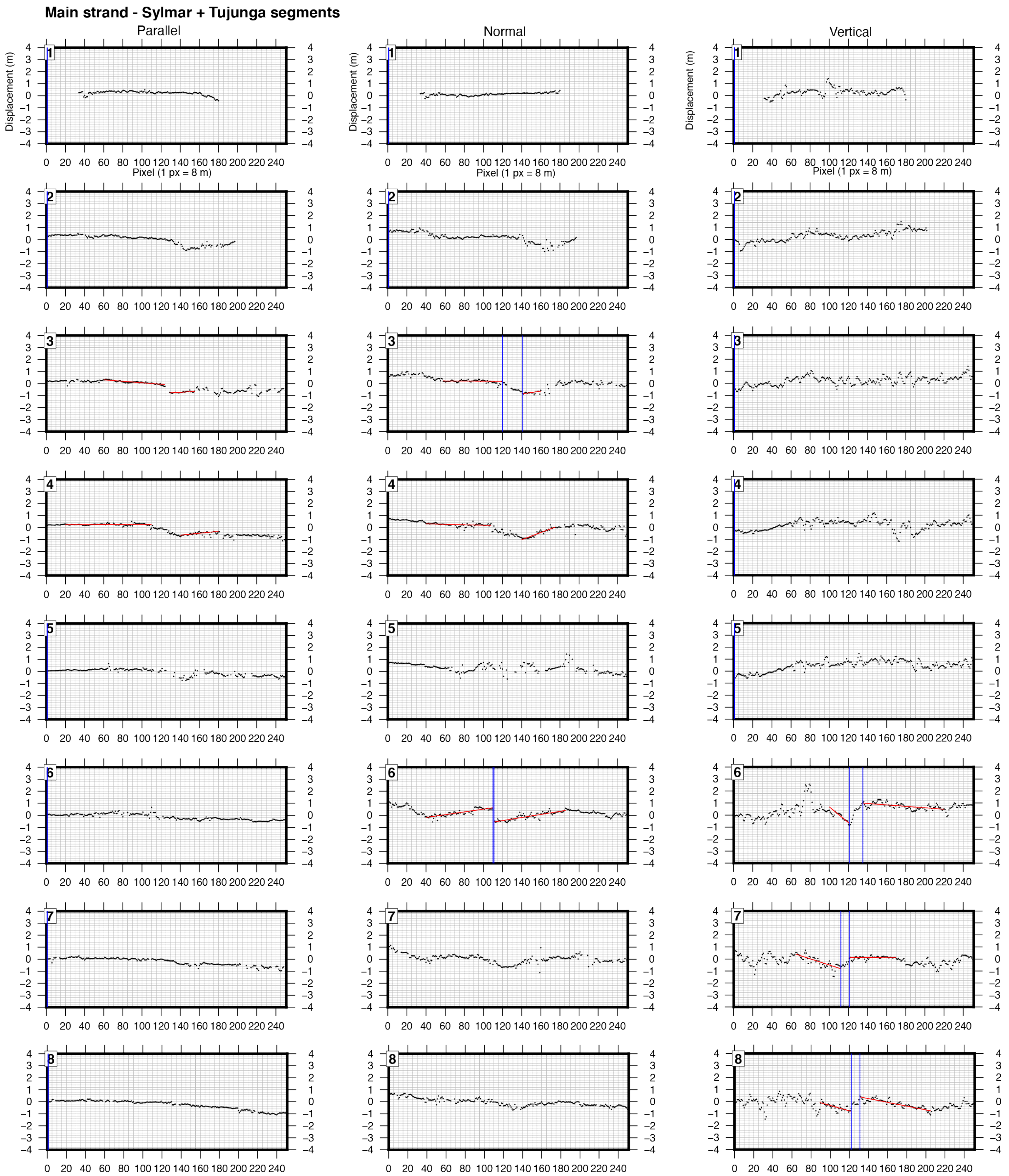

Figure S2. Strike-perpendicular coseismic displacement profiles from an averaged swath of a 21 pixel width. All profiles are as labeled on the first row of each page; displacement (m) as a function of fault-perpendicular distance (px). Numbers correspond to locations in Figure S1. Red lines represent linear regression and blue lines are placed at the boundaries of the preferred deformation zone.

Main strand - Sylmar + Tujunga segments

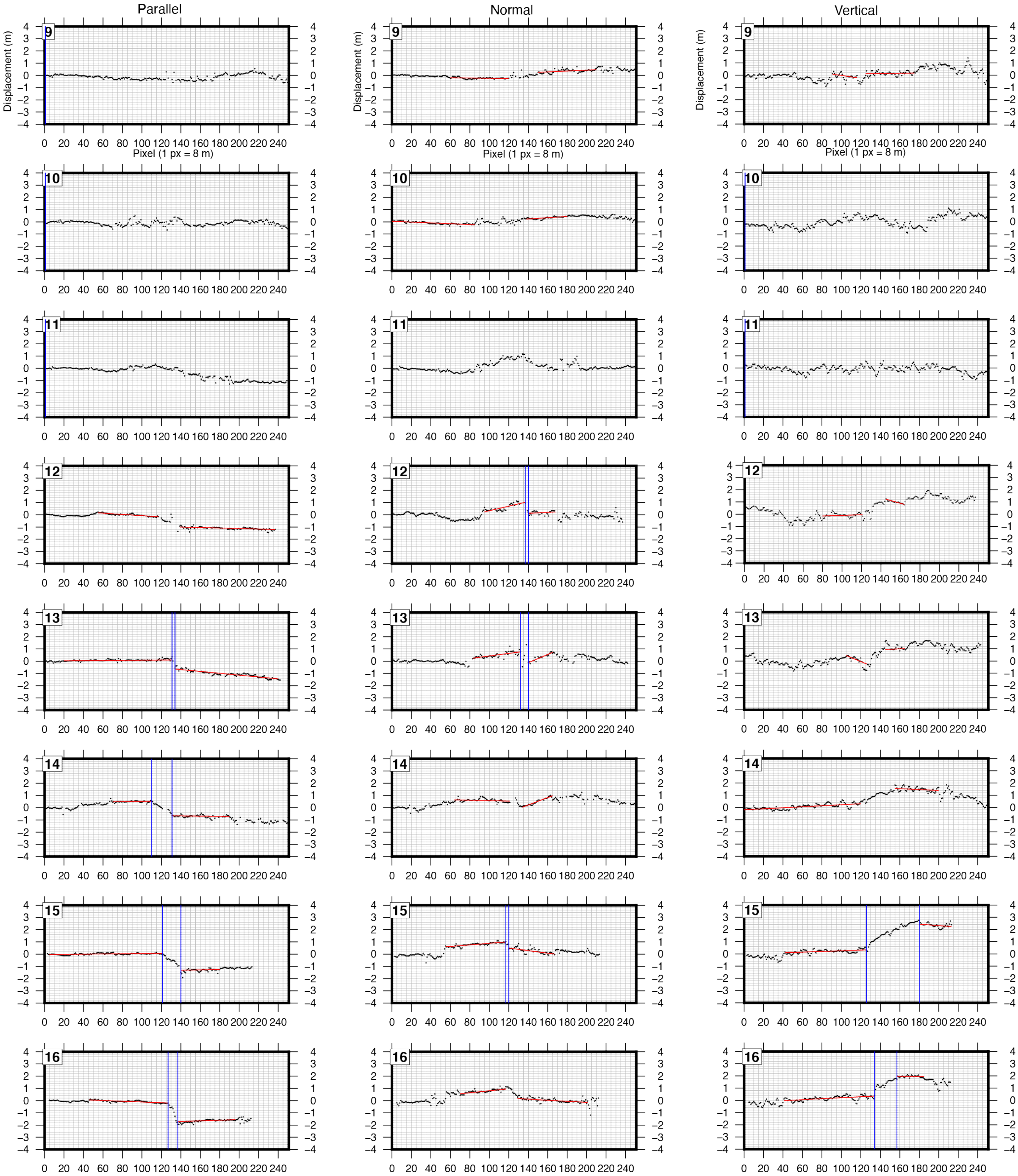

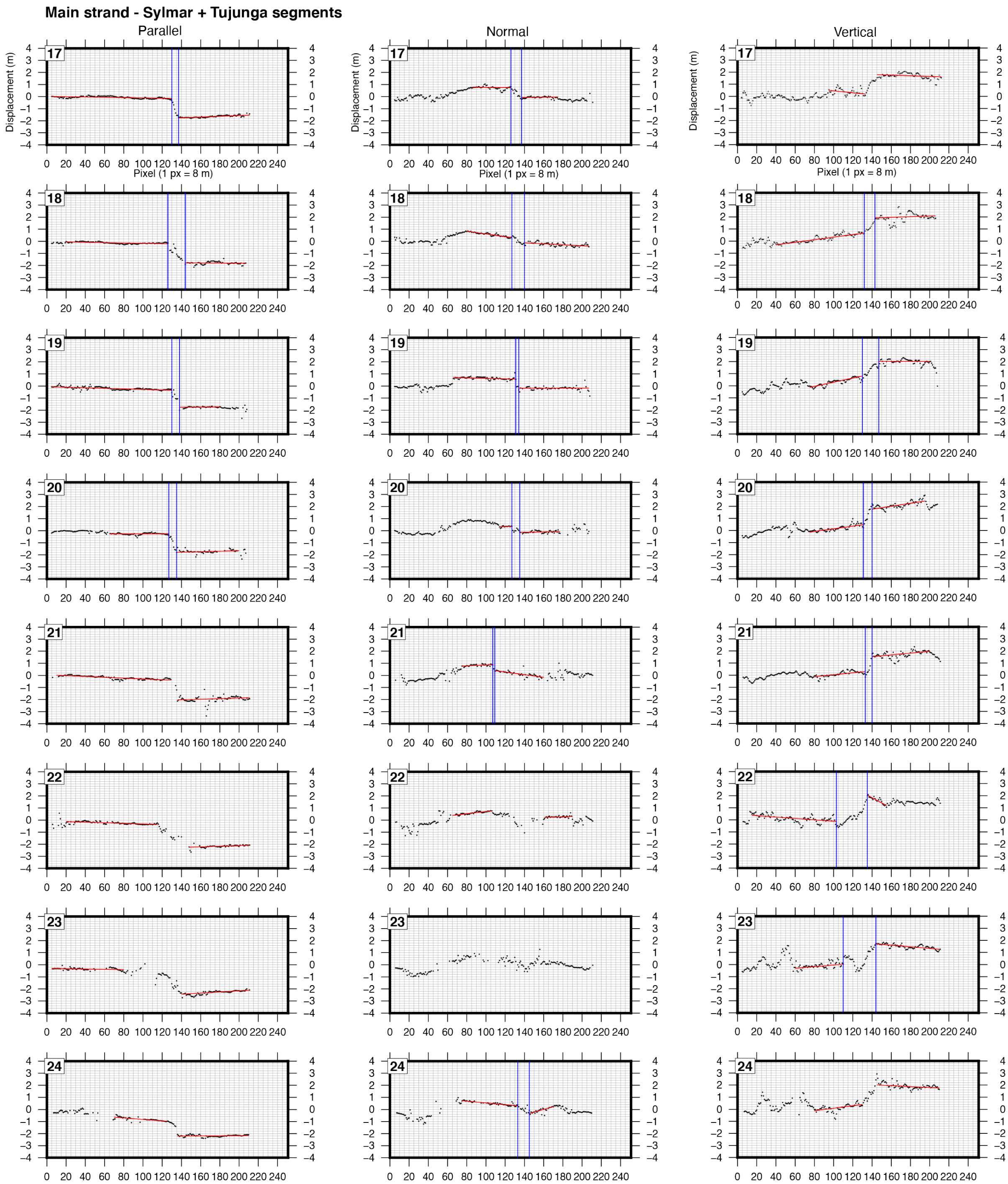
Main strand - Sylmar + Tujunga segments
Parallel
Normal
Vertical
Displacement (m)
Pixel (1 px = 8 m)
17
18
19
20
21
22
23
24

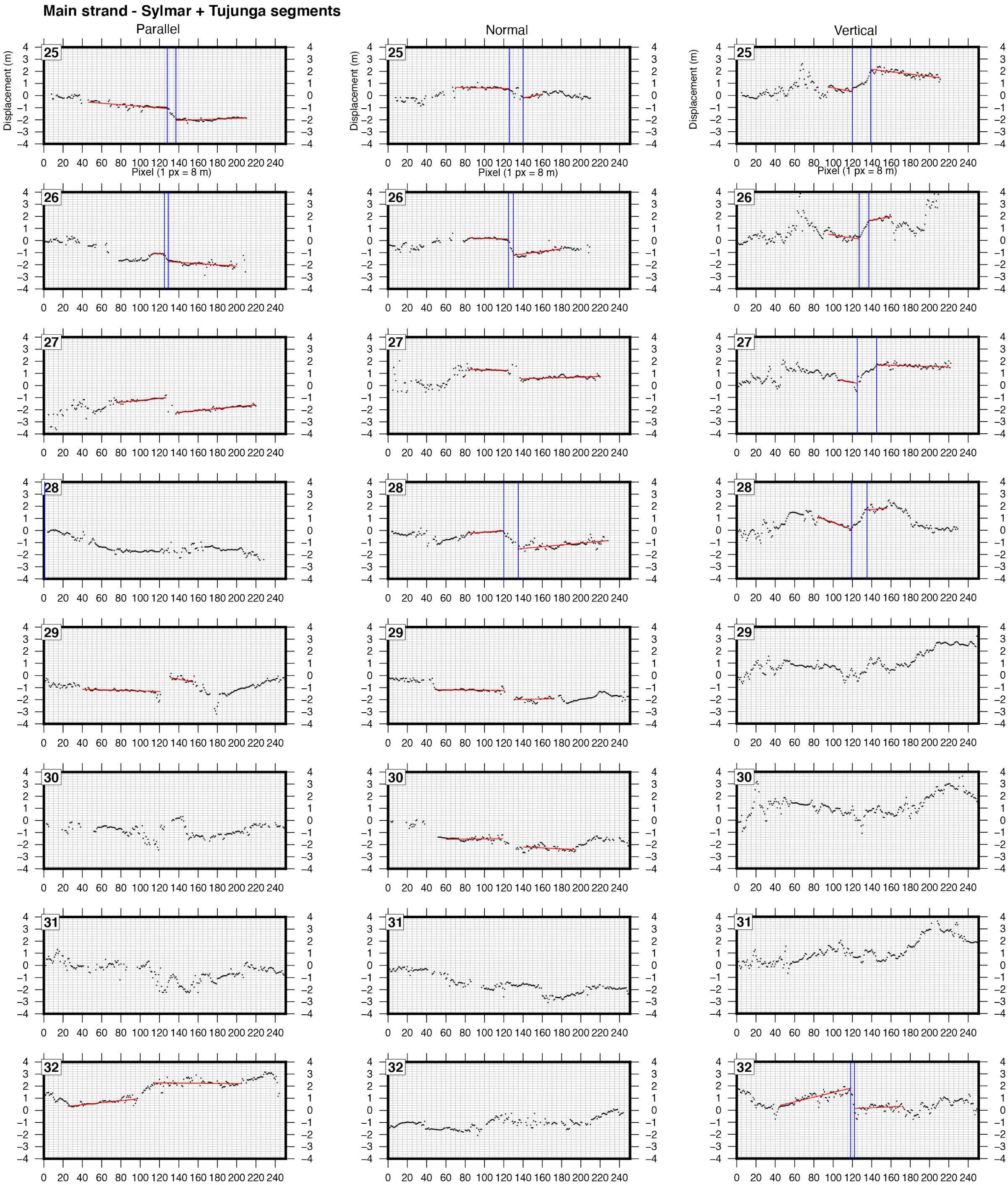
Main strand - Sylmar + Tujunga segments
Parallel
Normal
Vertical
Displacement (m)
Pixel (1 px = 8 m)
25
26
27
28
29
30
31
32

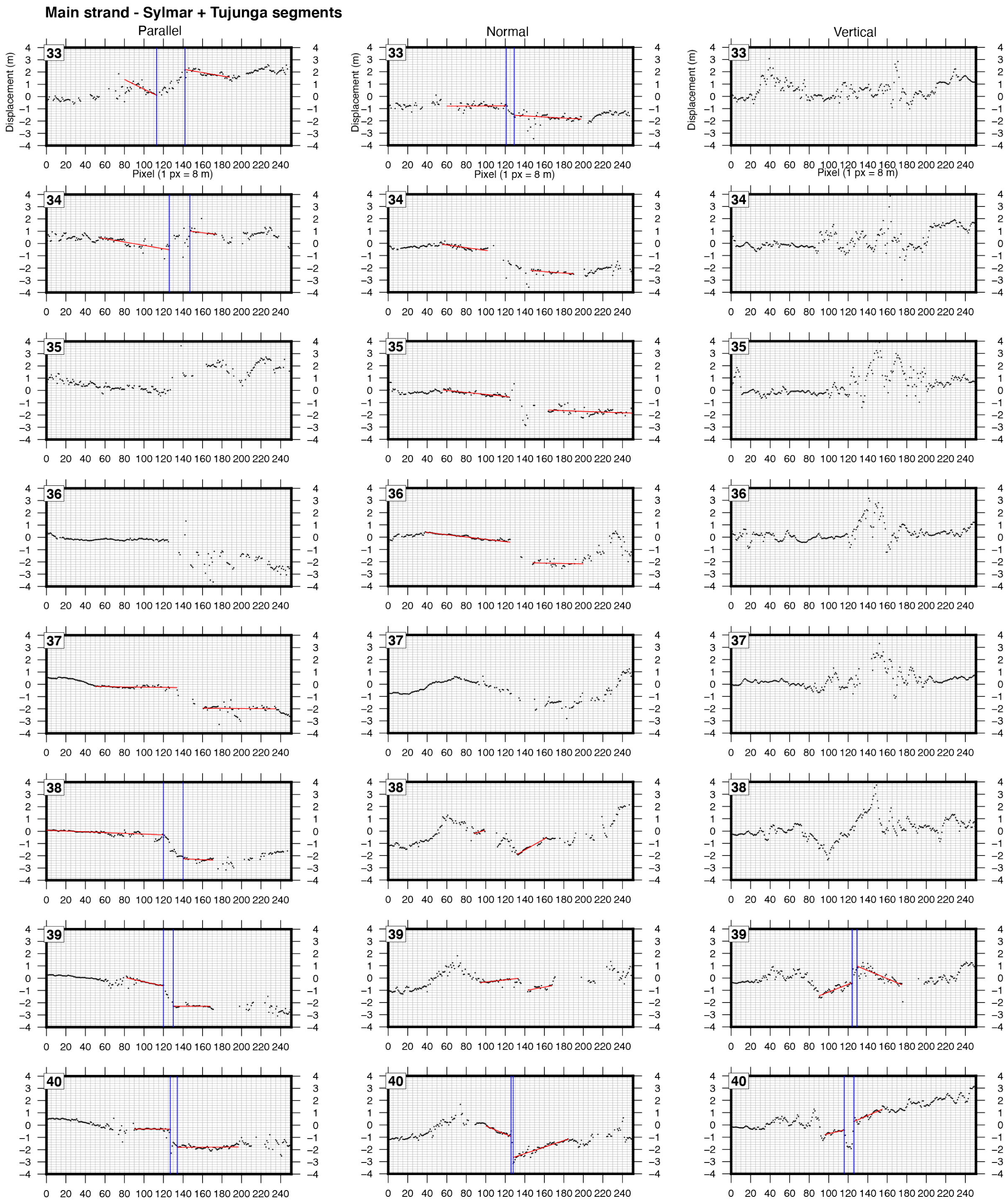
Main strand - Sylmar + Tujunga segments
Parallel
Normal
Vertical
Displacement (m)
Pixel (1 px = 8 m)
33
34
35
36
37
38
39
40

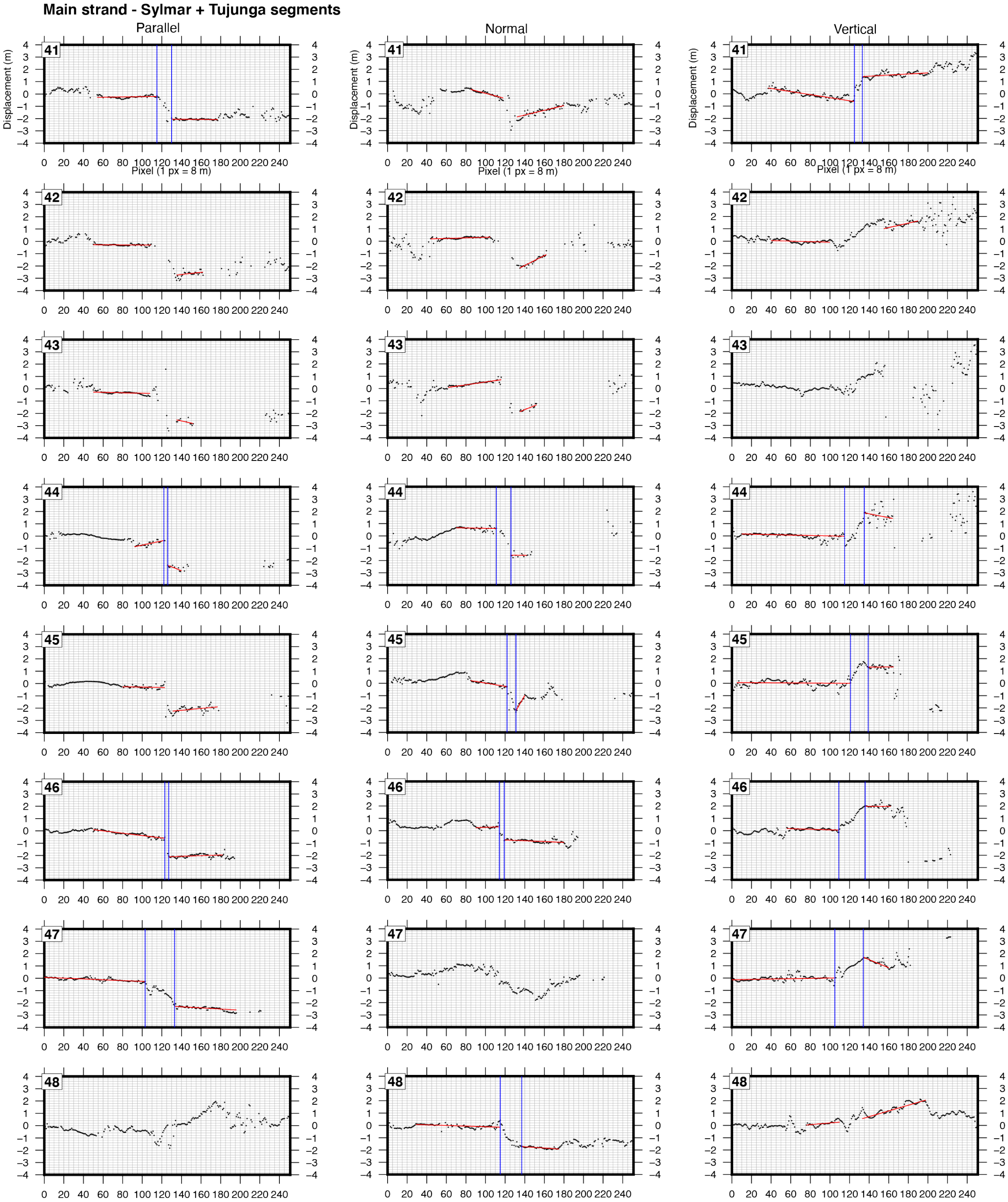
Main strand - Sylmar + Tujunga segments
Parallel
Normal
Vertical
Displacement (m)
Pixel (1 px = 8 m)
41
42
43
44
45
46
47
48

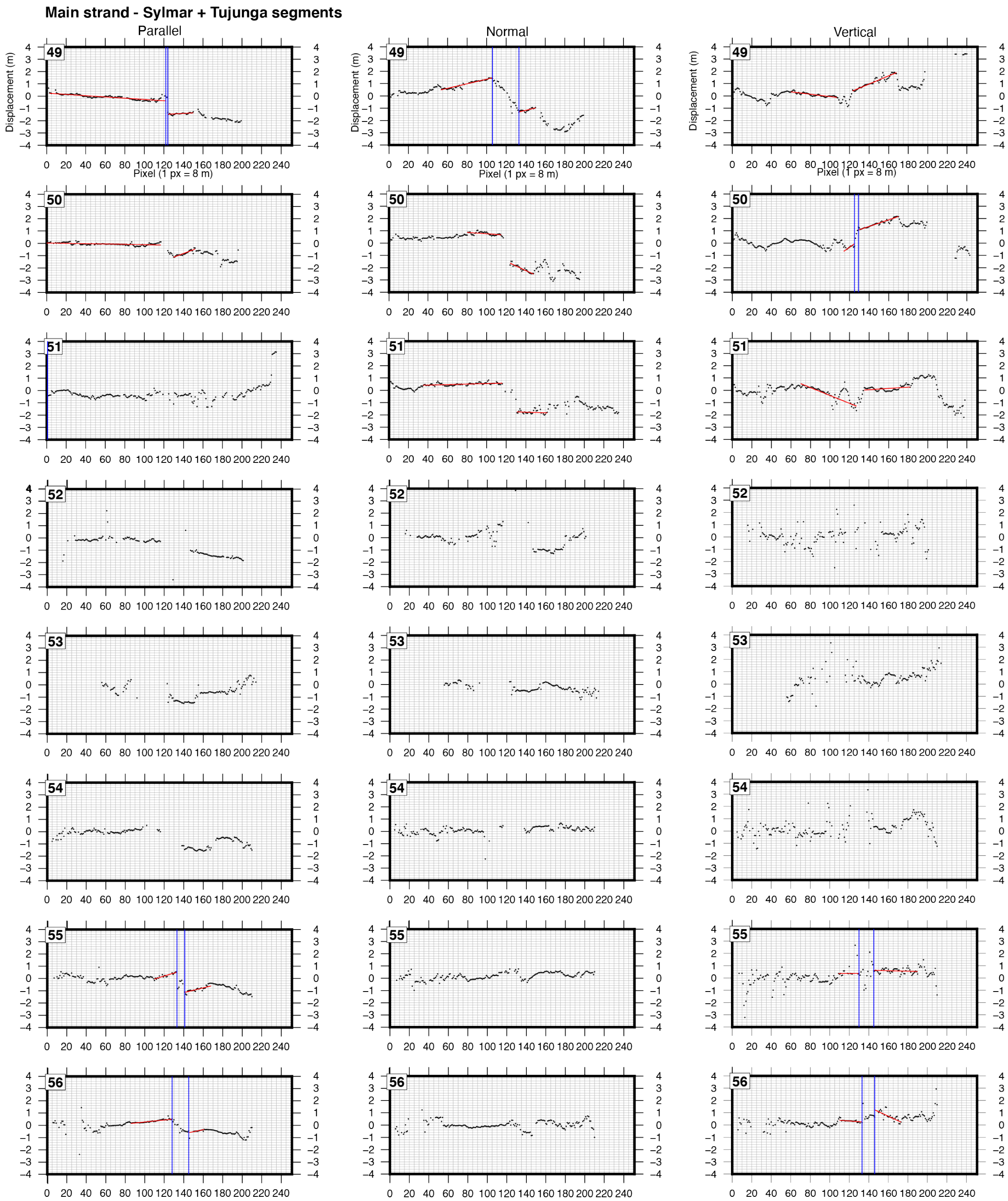
Main strand - Sylmar + Tujunga segments
Parallel
Normal
Vertical
Displacement (m)
Pixel (1 px = 8 m)
49
50
51
52
53
54
55
56

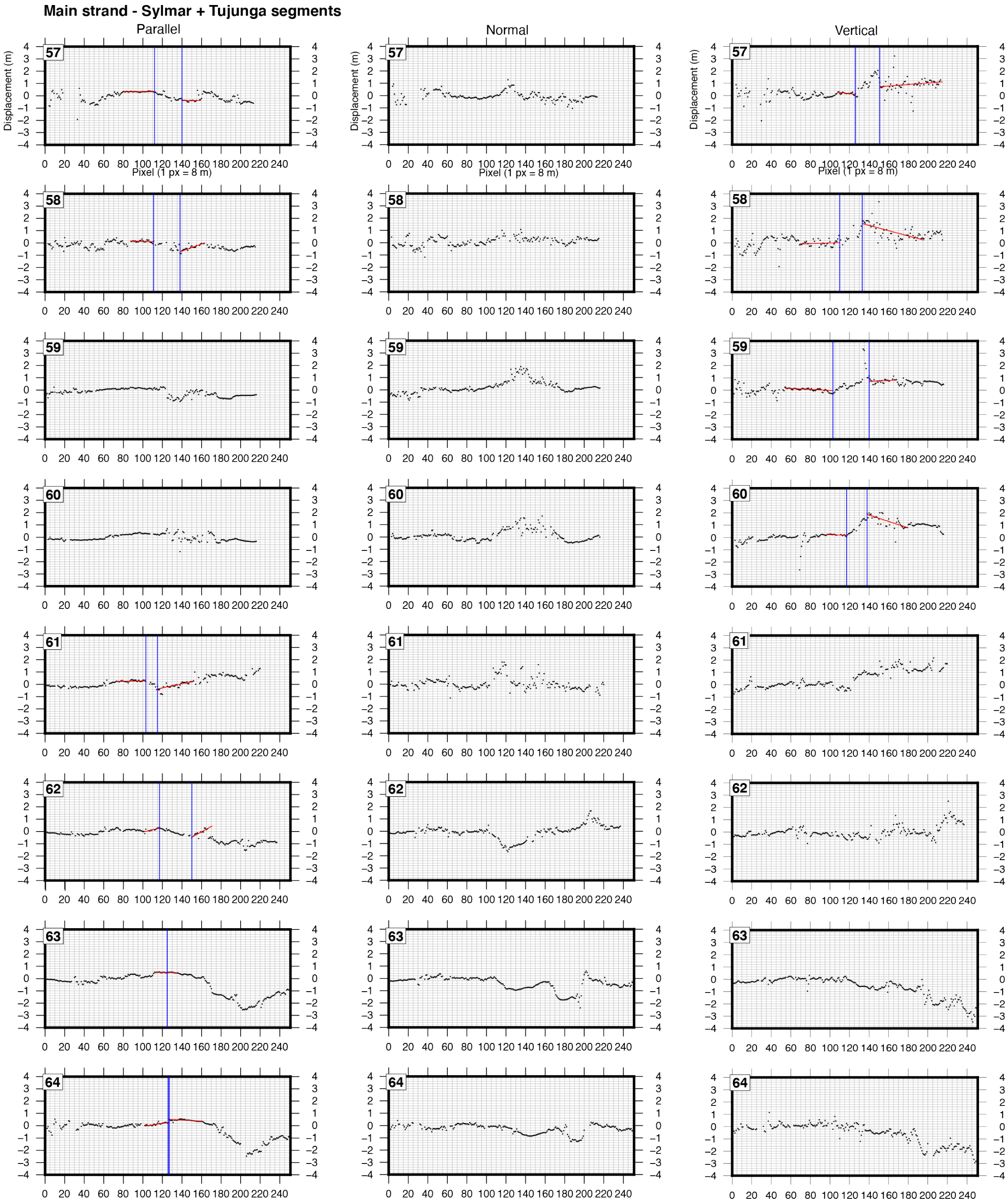
Main strand - Sylmar + Tujunga segments
Parallel
Normal
Vertical
Displacement (m)
Pixel (1 px = 8 m)
57
58
59
60
61
62
63
64
0 20 40 60 80 100 120 140 160 180 200 220 240
4 3 2 1 0 −1 −2 −3 −4

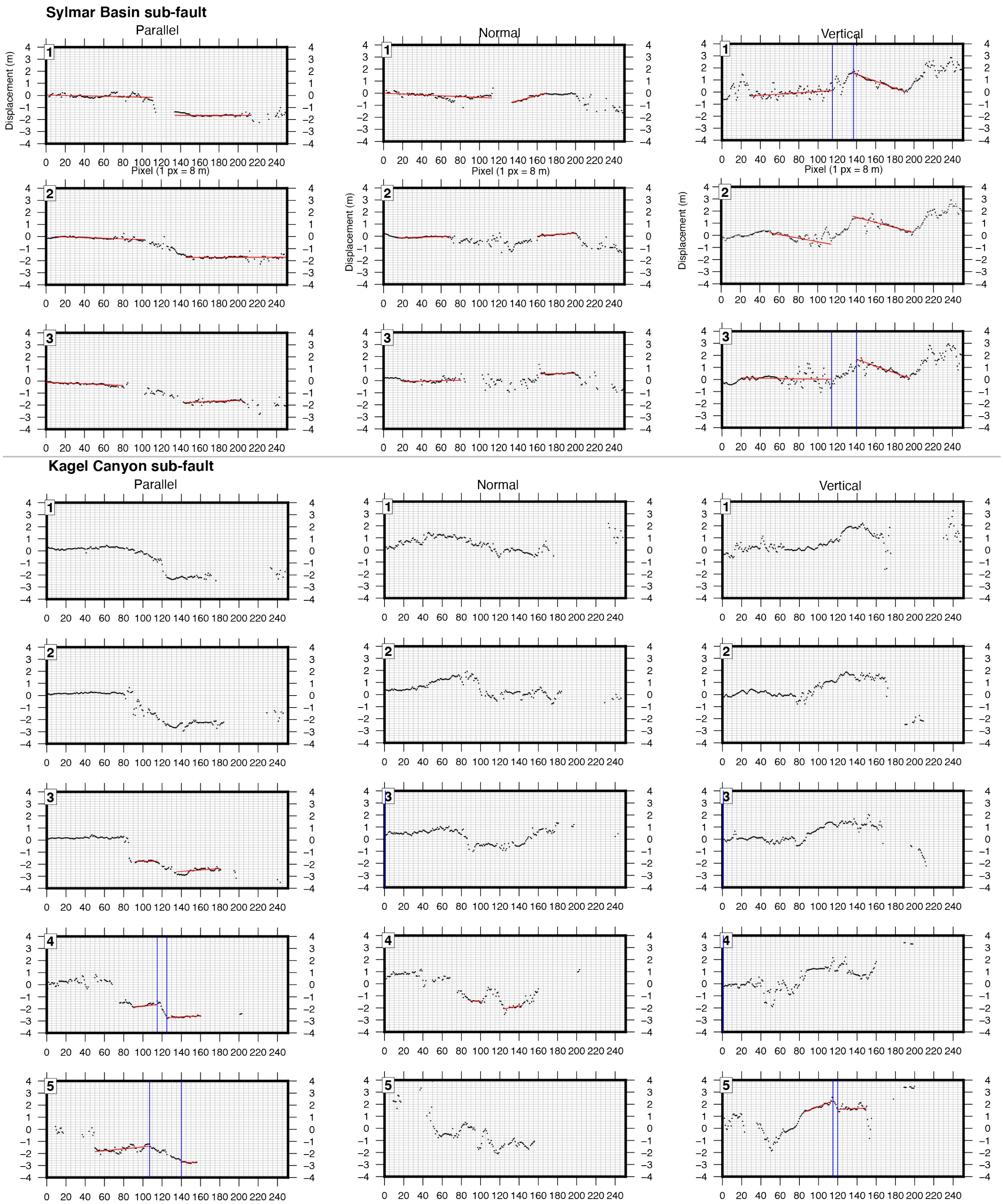
Sylmar Basin sub-fault
Parallel
Normal
Vertical
Displacement (m)
Pixel (1 px = 8 m)
Kagel Canyon sub-fault
Parallel
Normal
Vertical

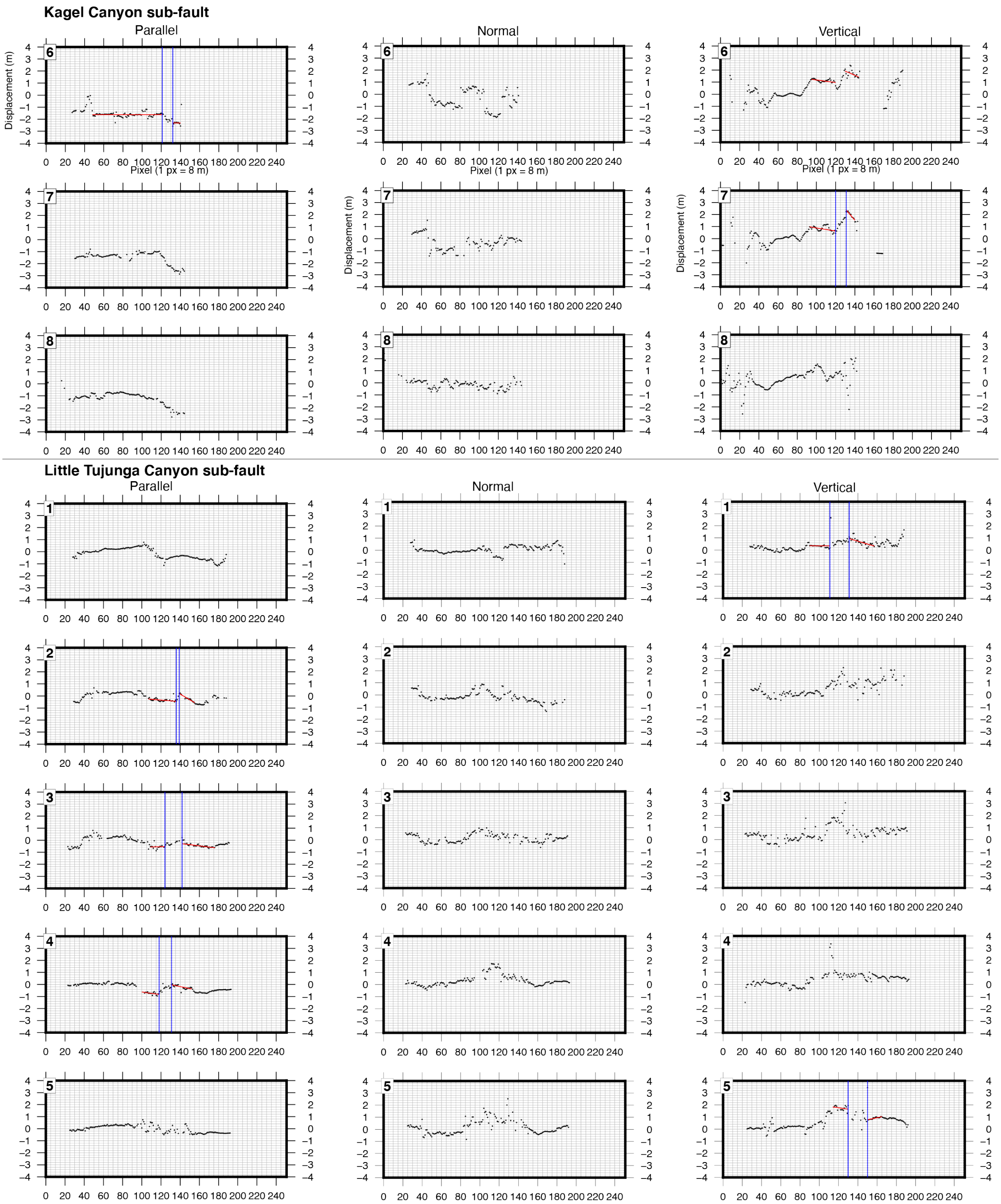
Kagel Canyon sub-fault
Parallel
Normal
Vertical
Displacement (m)
Pixel (1 px = 8 m)
6
7
8
Little Tujunga Canyon sub-fault
Parallel
Normal
Vertical
1
2
3
4
5

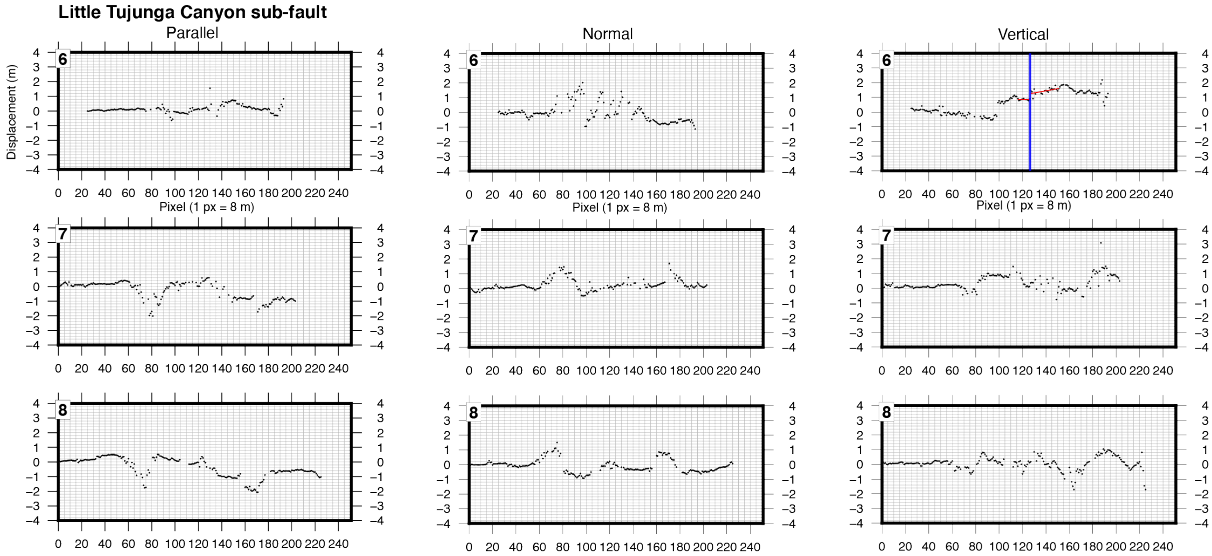
Little Tujunga Canyon sub-fault
Parallel
Normal
Vertical
Displacement (m)
Pixel (1 px = 8 m)
6
7
8

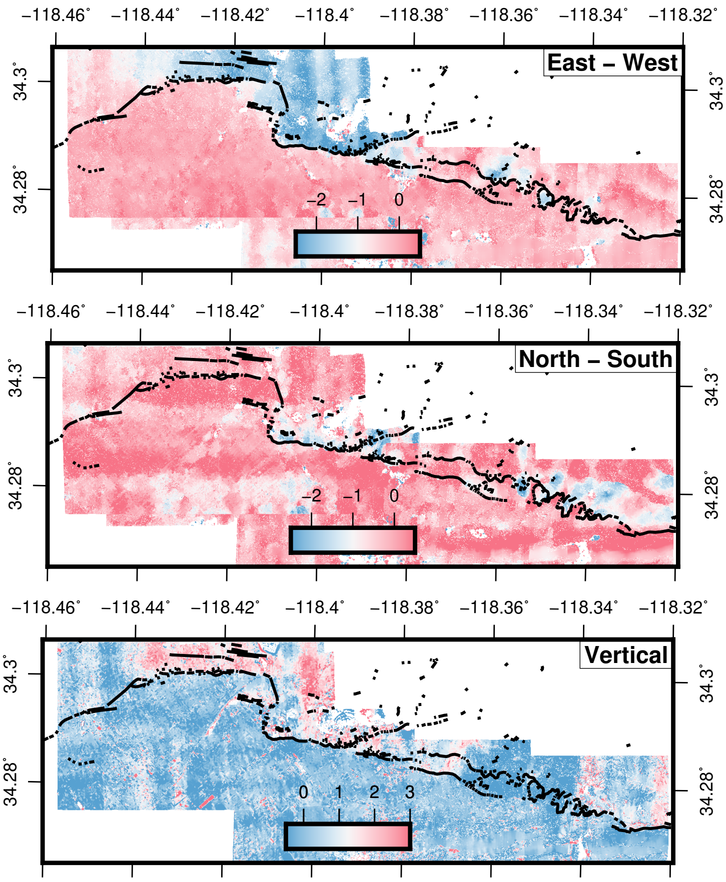

Figure S3. Full 3-D displacement field in meters.